geosciences

MDPI

Article

Zircon Isotopic Constraints on Age, Magma Genesis, and Evolution of the Betic Ophiolites, Nevado-Filábride Complex, Spain

Encarnación Puga [1], Antonio Díaz de Federico [1,†], Miguel A. Díaz Puga [2] and José Miguel Nieto [3,*]

[1] Instituto Andaluz de Ciencias de la Tierra CSIC, Avda. de las Palmeras 4, 18100 Armilla, Granada, Spain
[2] Espacio Natural de Sierra Nevada, Consejería de Sostenibilidad y Medio Ambiente, Junta de Andalucía, Carretera Antigua de Sierra Nevada, Km 7, 18191 Pinos Genil, Granada, Spain
[3] Department of Earth Sciences, University of Huelva, 21007 Huelva, Spain
* Correspondence: jmnieto@uhu.es
† Deceased, 29 February 2020.

Abstract

Metabasic rocks (eclogites and amphibolites) from four Betic ophiolite outcrops (Lugros, Almirez, Cóbdar, and Algarrobo), comprising Ol-Px gabbros, dolerites, and MORB-affinity basalts, were studied. U-Pb SHRIMP zircon dating yielded Early to Middle Jurassic ages (187–174 Ma). At Cóbdar and Algarrobo, several magmatic levels were identified (187 ± 1.7 to 174 ± 1.8 Ma, and 184 ± 1.8 to 180 ± 1.6 Ma, respectively). In Lugros, two gabbros were dated to 187 ± 2.5 and 184 ± 1.4 Ma, while a dolerite dyke intruding serpentinites in Almirez gave 184 ± 1.6 Ma. Algarrobo xenocrystic zircons, predominantly Precambrian, resemble those from the MAR (13° N–15° N) in age and chemistry, suggesting a similar tectonic setting. $\delta^{18}O$ values (4.2–6.2‰) of Betic ophiolite zircons (gabbros, basalts, dolerites) match those of MAR and SWIR samples, reflecting also oceanic alteration. Some zircons preserve $\delta^{18}O$ variations linked to Jurassic (~150 Ma) oceanic metamorphism and later orogenic overprints. REE patterns show depletions in HREE and Y, with localized enrichments in LREE and Hf, which are more marked in metamorphically recrystallized zones. Xenocrystic zircons may derive from Precambrian protoliths assimilated during Jurassic magma ascent near transform faults. This integrated geochronological and geochemical evidence provides the key constraints for a revised geodynamic framework, confirming the existence of a Betic Jurassic ocean basin, which is a crucial precursor to the Alpine orogenic events that shaped the region.

Keywords: Betic ophiolites; Nevado-Filábride Complex; U-Pb zircon geochronology; zircon $\delta^{18}O$ isotopes; zircon REE geochemistry

check for updates

Academic Editor: William M. White

Received: 31 August 2025
Revised: 4 October 2025
Accepted: 17 October 2025
Published: 20 October 2025

Citation: Puga, E.; Díaz de Federico, A.; Díaz Puga, M.A.; Nieto, J.M. Zircon Isotopic Constraints on Age, Magma Genesis, and Evolution of the Betic Ophiolites, Nevado-Filábride Complex, Spain. *Geosciences* **2025**, *15*, 406. https://doi.org/10.3390/geosciences15100406

Correction Statement: This article has been republished with a minor change. The change does not affect the scientific content of the article and further details are available within the backmatter of the website version of this article.

Copyright: © 2025 by the authors. Licensee MDPI, Basel, Switzerland. This article is an open access article distributed under the terms and conditions of the Creative Commons Attribution (CC BY) license (https://creativecommons.org/licenses/by/4.0/).

1. Introduction

The Betic ophiolites are the only preserved relics of the westernmost end of the Tethys Ocean, which developed from the Lower to Middle Jurassic (187–174 Ma), just at the beginning of the Pangaea breakup between the Iberia–European and the Africa–Adrian plates. Breakup and oceanization isolated continental remnants, known as the Mesomediterranean Terrane or AlKaPeCa (Alboran, Kabylies, Peloritani, Calabria) microplate [1,2], whose western end, forming the Alboran Block, was deformed and affected by high-pressure metamorphism. This metamorphism was due to the subduction of the Jurassic oceanic lithosphere and its related continental margins, with some relics of the subducted slab later

being exhumed and creating the Betic ophiolites of the Mulhacen Complex [3]. The Alboran block, formed by the internal zones of the Betic–Rifean Cordilleras, was later displaced toward the SW as a consequence of the opening of the extensional Argelian–Provençal Basin and the Alboran Sea [4,5]. Meanwhile, the eclogitized and partly exhumed ophiolites, forming part of the metamorphic Nevado-Filábride Complex of the Betic Cordillera, underwent a collision stage between the Iberian and African plates, which led to new metamorphic and deformational processes partly transforming the eclogites into amphibolites and greenschists [6].

The aim of this paper is the microscale U-Pb SHRIMP zircon study of the main outcrops of the Betic ophiolites and the geochemistry of their hosting rocks, in order to elucidate the age of their different oceanic magmatic levels and the chemical and isotopic characteristics of their zircons (U/Th, $\delta^{18}O$, Pb and U isotopic ratios, REE, and other trace elements), and to constrain their genetic conditions and later evolution. This study is mainly devoted to the central and easternmost ophiolitic outcrops of the Betic Chain (Cóbdar and Algarrobo; Figure 1) in order to compare them with the known outcrops, in some aspects, of the westernmost end of the Nevado-Filábride Complex (Lugros and Almirez; Figure 1). Based on this comparison, it is possible to elucidate the accretion age and development of the Betic oceanic floor along its total extension, from W to E, during the Jurassic.

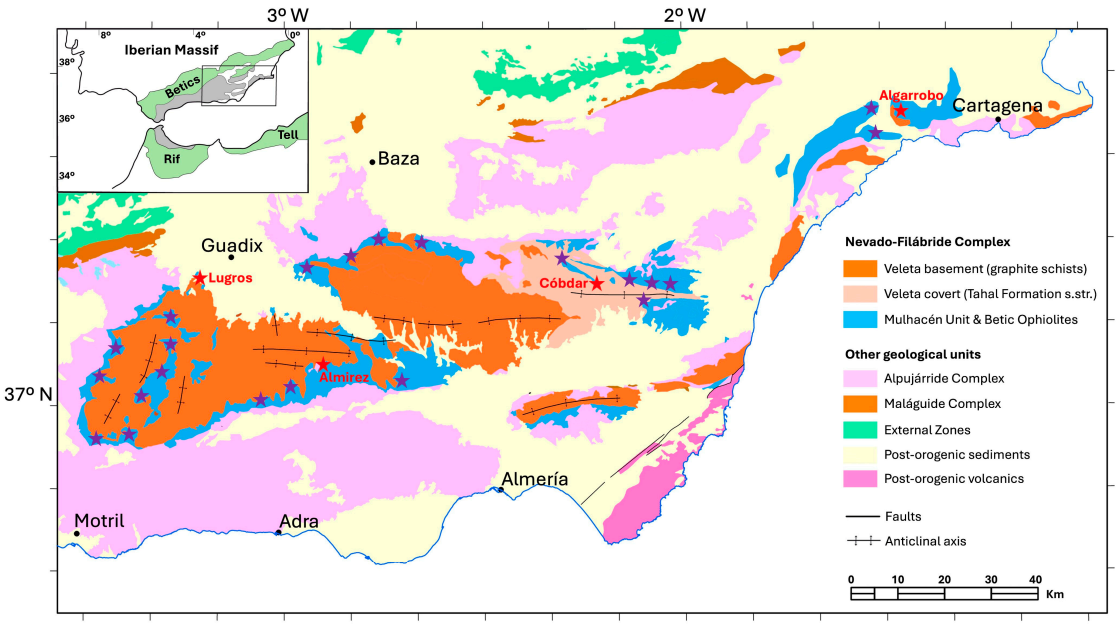


Figure 1. Geological sketch map of the central–eastern sector of the Betic Chain showing the main geological units, from Mapa Geológico de España 1:50,000 (IGME). The red and purple pointed stars represent the location of the main ophiolitic outcrops from which most of the studied rocks, discussed in Ref. [3] and in this paper, derive. The four ophiolitic outcrops from which the main part of the zircons studied in this paper come are in red.

Previous studies of the ophiolitic rocks in the Nevado-Filábride Complex were hindered by two primary factors: limited geochronological data [3,7] and a controversial division of its constituent units [6]. These limitations restricted the reliability of complex-scale conclusions because of the challenge to correlate different units across the complex, the scarce number of available dates, and the lack of documented zircon geochemistry, which is essential for interpreting their genesis and distinct recrystallization stages. This study addresses these gaps by providing a subdivision of the Nevado-Filábride Complex that can be correlated throughout the complex. Consequently, our work allows the geochemical,

geochronological, and geodynamic implications derived from the studied Betic ophiolites to be robustly extended to the entirety of the Nevado-Filábride Complex.

In the present work, we will compare new zircon results, in the higher part of the ophiolitic sequence from Cóbdar and Algarrobo outcrops, with those previously published from Lugros and Almirez, in order to establish the accretion age and temporal evolution along the Jurassic Betic oceanic floor, mainly based on geochemistry and the age of the zircons deriving from these four outcrops. The timing of the opening and nature of the crust, such as the development and life span of this Betic oceanic domain, are crucial to understanding the Mesozoic evolution of the westernmost Alpine Tethyan realm and the breakup between the Europa–Iberia and Adria–African passive margins [7–9].

2. Geological Setting

The Betic Chain, located in the southern part of the Iberian Peninsula, represents a key segment of the westernmost Mediterranean Alpine orogen [10], and has been traditionally divided into two main zones: the Internal and External Zones [11]. Within the Internal Zone, the Nevado-Filábride Complex, the deepest tectonic complex, hosts the Betic ophiolites [3].

The geology and tectonic subdivision of the Nevado-Filábride Complex (NFC) has been the subject of debate for the past 70 years. One of the main reasons for the lack of consensus among researchers working on the NFC lies in the nature of the early geological studies. Detailed surveys, including geological mapping, conducted in the 1960s and 1970s focused on partial sections of the complex, either in the Sierra Nevada or in the Sierra de los Filabres. As a result, each study proposed a set of locally defined units, making their correlation across the NFC challenging.

In this study, we adopt, with minor terminological adjustments, one of the latest essays in the definition of tectonic units of the NFC [12], integrating prior subdivision schemes from both the Sierra de los Filabres [13] and the Sierra Nevada [6] sectors. This subdivision of NFC units relies critically on (1) the nature and metamorphic evolution of the graphite-bearing basements of the NFC continental units (see Table 1 of Ref. [13]), which serve as diagnostic markers, and (2) the Maximum Depositional Ages (MDAs) of their graphite-free pelitic and psammitic covers, which provide additional stratigraphic constraints [14]. With this scheme, three major units can be distinguished in the NFC from bottom to top:

The Lower Unit (LU), which we rename here the Veleta Unit for consistency with our previous work [6], and because the graphite schists of this LU are those outcropping at Veleta Peak (3398 m) in the Sierra Nevada, correlates with the Nevada I and Nevada II units of Ref. [13] and the Aulago Formation of Ref. [15], later renamed the Ragua Unit [16]. The LU essentially corresponds to what in the pioneering studies of the NFC was termed the 'Sierra Nevada Series' [17–19]. Overlying the LU is the 'Mischungszone' or 'Mixed Zone' identified in these pioneering studies, which basically encompasses mainly the NFC's two other units: the Intermediate and Upper Units.

The basement of the LU consists of a highly monotonous sequence of graphitic schists over 5000 m thick, with increasingly abundant intercalations of quartzite layers towards the top of the succession. A distinctive feature of the graphitic schists in the basement of the LU is their petrological monotony and the systematic absence of other lithotypes commonly found in the basements of higher continental units, such as tourmaline gneisses, amphibolic gneisses, and skarn rocks, as we will discuss later. This fact, clearly shown in the detailed mapping studies of the NFC [13], has nevertheless been overlooked by some recent authors when subdividing the NFC, despite the LU basement being widely exposed in the core of the Sierra Nevada and Sierra de los Filabres antiforms, where the presence of these lithotypes (tourmaline gneisses, amphibolic gneisses, and skarn rocks) has never

been documented. The age of these basement materials is Devonian–Carboniferous [20,21] or older, with a maximum depositional age in the Carboniferous [14].

Unconformably overlying the graphitic schist basement is a sequence of graphite-free metapelites and metapsammites, beginning with a basal metaconglomerate. This LU cover corresponds to the Tahal Formation, as originally defined by the first detailed studies of the Sierra de los Filabres [22,23], where it is best exposed. A significant source of uncertainty in later studies of the NFC has been the inconsistent use of the term Tahal Formation, not only for the LU cover as initially defined, but also for other graphite-free metapelitic rocks in higher tectonic units, to which the original authors [22,23] assigned, in fact, different names (e.g., Colmenica Schists, Almendros Schist, Malea Schist, etc.). This confusion has further complicated attempts to correlate NFC units, as the Tahal Formation in many later works encompasses metasedimentary sequences of varying ages and origins. For example, some authors [14,16] grouped all NFC graphite-free metapelites under this name, yet only those matching the original Tahal Formation definition [22,23] exhibit Permian MDAs (the LU cover) [14], while higher-unit metapelites, also called the Tahal Formation [14,16], yield Triassic–Jurassic MDAs [14].

Both the basement and the cover of the LU exhibit intermediate pressure–temperature metamorphism, ranging from Ab-Ep amphibolite to greenschist facies [6]. As highlighted by Ref. [13], a distinctive feature of the LU's metamorphism compared to other NFC continental units is the systematic absence of phases such as staurolite and kyanite, while chloritoid is frequently present. In contrast, staurolite and kyanite are common phases in the schists (with or without graphite) of the overlying units. In the same way, Ref. [24] highlights that both microstructural analysis and pre-Cenozoic apatite U-Pb ages suggest that the LU endured lower temperatures than the other units of the NFC, likely below 450 °C.

The Middle Unit (MU) is arguably the most controversial subject among researchers studying the NFC. While the ophiolitic nature of its mafic and ultramafic rocks was recognized early [25], and was even suggested in the pioneering studies of the NFC [26], only recently has it been established that these rocks form an ophiolitic mélange [12], similar to those documented in many accretionary- and collisional-type orogenic belts worldwide [27]. According to Ref. [12], this (ultra)mafic mélange cannot be dismissed as a mere brittle shear zone mixing different lithologies, as some outcrops still preserve their original sedimentary olistostrome fabric, albeit having been overprinted by later shearing during burial and further disrupted by extensional shear zones and normal faults during exhumation. These authors also argue that interpreting this MU as an ophiolitic mélange linked to obduction does not preclude the coexistence of a hyper-extended continental margin [28], where the continental mantle may have transitioned into a narrow or incipient oceanic lithosphere, scenarios that in fact could be part of the same paleogeographic domain.

The stratigraphic, structural architecture, and lithological composition of ophiolitic mélanges are inherently complex [27], as exemplified by the MU of the NFC. This Middle Unit contains not only mafic and ultramafic protoliths but also metapelites and marbles of diverse origins, exhibiting varying degrees of metamorphism and deformation. Among the mafic rocks, where metamorphic and deformational effects are most evident, the MU displays the full spectrum of scenarios, from olivine gabbros preserving their original igneous textures and mineralogy to amphibolites with planar–linear fabrics, including both deformed and non-deformed (i.e., with igneous textures) eclogites. While this variability has attracted considerable attention from most researchers working on the NFC, it is in fact a common feature of ophiolitic mélanges [27], where rocks that underwent subduction and high-pressure metamorphism may coexist within the same outcrop, with non-subducted rocks retaining their primary igneous texture and mineralogy.

A distinctive feature of some metasedimentary rocks in this MU is the occasional occurrence of chromium-rich layers (ranging from millimeter to centimeter scale), observed both in calc-silicate rocks [29] and in metapelites. Notably, the metapelitic sequences sometimes contain chromium-enriched levels that exhibit remarkable lateral continuity, traceable for more than 1 km, suggesting very limited mobility of this element during metamorphism, as was also pointed out by Ref. [29].

The age of the ophiolitic magmatism has been determined as Lower to Middle Jurassic (187–174 Ma) based on U-Pb zircon dating in Ref. [3] and this study, while the metasedimentary rocks of the MU yield Triassic and Jurassic MDAs [14]. Moreover, metasediments (quartzites, micaschists, and calcschists) overlying the (ultra)mafic successions have been interpreted as part of a pelagic sequence formed on the ocean floor during the Cretaceous [30].

There is broad consensus among all authors regarding the metamorphic conditions of the LU, as previously discussed, ranging from albite–epidote amphibolite to greenschist facies. However, for the overlying units, there is significant variability in P-T condition estimations depending on the rock type, the assigned unit of the studied sample, and other factors, as highlighted in a recent review of the NFC metamorphism [31].

A major source of these discrepancies stems from the fact that only very recently has the existence of an ophiolitic mélange within the NFC been recognized [12]. In most prior studies on the NFC, the basic and ultrabasic ophiolitic rocks of the MU were considered part of the continental sequences, and consequently, the PT estimates obtained from rocks of both the MU and the Upper Unit (UU) have been assumed to belong to the same unit. Nevertheless, the highest PT conditions reported so far in the NFC, ranging from 18 to 24 kbar and from 650 to 700 °C, correspond to basic and ultrabasic rocks of the MU, as well as to their associated metasedimentary rocks (metapelites and metaevaporites) [31]. Following peak pressure conditions, subsequent uplift led to a decompression path that remains poorly constrained. Most authors suggest that decompression occurred with initial heating, followed by slight cooling in the amphibolite facies [31].

The Upper Unit (UU) we rename here the Mulhacén Unit for consistency with our previous work [6] and because its graphite schists are the ones outcropping at Mulhacén Peak (3479 m) in the Sierra Nevada. The graphite schists of the basement of this unit correlate with the Nevada III and Nevada IV units of Ref. [13] as well as the Montenegro Formation of Ref. [15] and the Paleozoic rocks of the Calar Alto unit of Ref. [16].

The Upper Unit consists of two superimposed continental sequences, both comprising a graphite schist basement overlain by a cover of non-graphitic schists and marbles. For greater clarity in the following discussion, we will refer to the lower continental sequence of the UU as the Caldera Unit and the upper sequence as the Sabinas Unit, adopting traditional nomenclature from the Sierra Nevada [6], which also correlates well with detailed field studies from the Sierra de los Filabres, where they have been assigned different names by various authors [13,22,23]. These two continental sequences (Caldera and Sabinas) are extensively exposed with remarkable lateral continuity in the eastern part of the NFC, both on the northern and on the southern flanks of the Sierra de los Filabres antiform. In the Sierra Nevada, the same two continental sequences also outcrop [6], though in smaller, often highly deformed exposures with very limited lateral continuity. Additionally, especially in the Sierra de los Filabres, it is common to find basic and ultrabasic rocks from the MU's ophiolitic mélange, particularly the latter (serpentinites), intercalated at the contact between these two continental sequences [23].

A distinctive key feature of the graphitic schists in the basements of the Upper Unit is the systematic presence, in both the Sierra Nevada and the Sierra de los Filabres, of tourmaline gneisses, pyroxene rocks (skarns), or amphibole–epidote–biotite gneisses intercalated in the graphite schist sequences [6,13,22,23,32,33]. Based on field characteristics (outcrop type,

associated rocks, etc.) and petrographic, chemical, and mineralogical features, gneisses from the Upper Unit can be classified into two groups [32]: (1) peraluminous tourmaline gneisses of plutonic origin, which texturally range from metagranites to augen gneisses and even-grained gneisses, depending on the varying degrees of deformation and metamorphism affecting the original granites; and (2) metaluminous amphibole–epidote–biotite gneisses and weakly peraluminous tourmaline gneisses, for which a volcanic origin has been suggested, due to the absence of plutonic textures and because they occasionally occur as alternating bands within the same outcrop with high lateral continuity. Plutonic tourmaline gneisses predominantly occur in the basement of the Caldera Unit and are systematically associated with pyroxene-bearing rocks (skarns) within the graphite schists into which granites intrude. In contrast, amphibole–epidote–biotite gneisses and tourmaline gneisses, suggested to be of volcanic origin, are found both in the cover sequence of the Caldera Unit and in the basement and cover of the Sabinas Unit [32].

However, some authors [34,35] have proposed that only a single type of gneiss exists, with minor compositional variations, based on a very limited dataset and a rather simplistic petrologic discrimination approach using major-element oxide data in the de la Roche R1–R2 multicationic diagram [36] used for granitoid discrimination [37]. While this multicationic classification might be useful, relying exclusively on major elements oversimplifies the complex processes involved in granitoid formation and evolution. Moreover, since this classification primarily targets igneous rocks (both volcanic and plutonic), its application to metamorphic rocks, which may have undergone significant mineralogical and textural changes, becomes potentially problematic.

A more robust approach for discriminating the NFC gneisses should therefore employ classification schemes based on more immobile trace elements [38]. Indeed, when using these trace element discrimination diagrams, peraluminous plutonic tourmaline gneisses fall within the syn-collisional granitoid field, while the metaluminous amphibole–epidote–biotite gneisses and associated weakly peraluminous tourmaline gneisses consistently fall within the post-collisional granitoid field [32,39]. Furthermore, the Nd isotopic signatures of both gneiss groups are markedly distinct. Peraluminous plutonic tourmaline gneisses exhibit strongly negative initial ε_{Nd} values (around -6) typical of partial melting of metasedimentary sources, while the metaluminous amphibole–epidote–biotite gneisses and associated weakly peraluminous tourmaline gneisses display ε_{Nd}(i) values ranging from slightly negative (-2) to highly positive (+4.5), clearly indicating a mantle source with variable degrees of crustal contamination in the formation of the second gneiss type [32,39]. Such a distribution of ε_{Nd}(i) values is typical of continental rifting settings, as has been described in other regional contexts [40].

Several attempts have been made to date the magmatism responsible for both types of gneisses, though the results remain inconclusive. Excluding older studies, whose accuracy may be questionable, the obtained ages for the magmatism that formed these gneisses range from Late Carboniferous to Early Permian (314 to 276 Ma), a range also observed within both gneiss types [14,41]. Remarkably, even for the same site, a small gneiss outcrop (spanning a few hundred square meters) at Collado de las Sabinas in the Sierra Nevada, published ages vary significantly across studies: Ref. [42] determined an age of 301 $\pm$ 7 Ma (sample S00), while Ref. [14] established an age of 276.2 $\pm$ 0.3 Ma (sample 19SSN13). A similar situation occurs in other NFC gneiss outcrops, both in peraluminous plutonic tourmaline gneisses and in metaluminous amphibole–epidote–biotite gneisses and associated weakly peraluminous tourmaline gneisses, suggesting that further geochronological work would be required to establish both the precise age and the synchronous/diachronous character of the magmatism that generated these two gneiss types.

Metamorphism in the Upper Unit of the NFC exhibits a distinctly polyphasic character, with at least two well-defined phases: pre-Alpine metamorphism and Alpine metamorphism [6,31,41].

Pre-Alpine metamorphism is particularly well represented in the lower continental sequence (Caldera Unit) of the western NFC, where Paleozoic graphitic schists preserve pre-Alpine metamorphic assemblages such as chloritoid + almandine or andalusite ± staurolite + biotite + almandine. These pre-Alpine assemblages formed under static, low-pressure, intermediate-temperature conditions [6,41] and are later overprinted by Alpine high-pressure assemblages characterized by phengite + kyanite + Mg-rich chloritoid + pyrope-rich garnet [31].

The P-T conditions of Alpine metamorphism, however, remain somewhat unclear due to uncertainties in assigning the studied samples to the Upper Unit when reviewing the published data [31]. In cases where samples can be confidently attributed to the Upper Unit, estimated maximum peak metamorphic conditions range between 14 and 16 kbar and between 500 and 650 °C. Nevertheless, the unequivocal preservation of igneous plagioclase in metagranites from the Sierra de los Filabres [22,32] clearly indicates that the Upper Unit, at least in the eastern NFC, did not reach the jadeite stability field, implying maximum P-T conditions below 15 kbar at 550 °C. In contrast, as noted earlier, estimated P–T conditions for the Middle Unit lie well beyond the jadeite stability field. In fact, decimeter-sized pockets of exceptionally pure jadeite [43] can be found interbedded within metapelites of the ophiolitic mélange.

Another ongoing controversy regarding the NFC's stratigraphy and structure involves persistent disagreements about the cartographic distribution of its units. Given that outcrops of the ophiolitic mélange are typically small-scale relative to the entire complex, most authors have included them in NFC cartographic syntheses as part of the Upper Unit (Mulhacén Unit). However, there remains fundamental disagreement, particularly concerning the cartographic extent of the Lower Unit (Veleta Unit). The main differences among the various cartographic syntheses published to date primarily concern the central part of the NFC. In this area, the core of the Sierra de los Filabres antiform structure consists of a thick, monotonous series of graphitic schists, which some authors attribute to Mulhacén-type successions [16,21], while others argue for classification as Veleta-type successions [6,24]. However, detailed lithological and cartographic fieldwork in this region [44] confirms that these rocks align with Veleta-type successions, as supported in the same study. This interpretation is further reinforced by the systematic absence, across the vast mapped area, of key Mulhacén-type basement rocks, including metagranites, orthogneisses, and associated pyroxene-bearing rocks [13,44].

Finally, regarding the age of Alpine metamorphism in the NFC, a recent study synthesizes the key geochronological results published to date, along with new U-Pb apatite and zircon data (see Figure 9 in Ref. [24]). The study reveals that structurally higher levels of the NFC contain both Eocene and Miocene metamorphic zircon rims and apatite ages. Notably, the presence of Miocene apatite and zircon ages with metasomatic morphologies in the upper NFC record fluid-rich metamorphic conditions, potentially linked to Late Miocene extensional shear zones. These findings indicate that subduction must have initiated at least since the Eocene (~60 Ma), with progressive subduction and underplating of NFC units, reconciling prior discrepancies over subduction initiation and the wide range of metamorphic ages spanning from the Eocene to the Miocene [24].

3. Petrological Characterization of the Betic Ophiolites

Figure 1 shows, as pointed stars, the approximate position of the basic and/or ultramafic outcrops identified in previous works ([3] and references therein), as forming part of

the Betic ophiolites. The red names correspond to the outcrops (Lugros, Almirez, Cóbdar and Algarrobo) from which the main part of the zircons studied in this paper come from.

The location of the dated rocks from the Cóbdar outcrop is shown in Figure 2, together with those of other types of rocks that would complete the igneous rock succession, forming this outcrop before its subduction and metamorphism. This igneous lithologic comprises everything from gabbroic rocks at the bottom of the sequence (2CB, 3CB, 5CB samples), represented by microphotos A-1 and A-2, in Figure 3, to doleritic dykes and basaltic-type layers with pillow lavas, which form the top part of the igneous series, represented by samples 4CB, 6CB, and FACO-24 (or J-Anf-SS), to which microphotos A-3 and A-4 in Figure 3 correspond, respectively. These higher volcanic layers commonly form sills, in contact with or intercalated between the basal layers, in the overlying meta-sedimentary cover located on the igneous succession. The basaltic level also presents pillow structures (P in Figure 2), varying in diameter from one decimeter to a meter size, that are well represented in the ECO-8 and 4CB outcrops (see the macrophotos in Figure 3c-2 of Ref. [3]). These pillows present inner vesicles that may be later filled by phlogopite, brown amphibole, albite, and epidote of oceanic and later orogenic metamorphism (microphoto A-3 in Figure 3) and are traversed by scarce dolerite dykes (sample PECO-105).

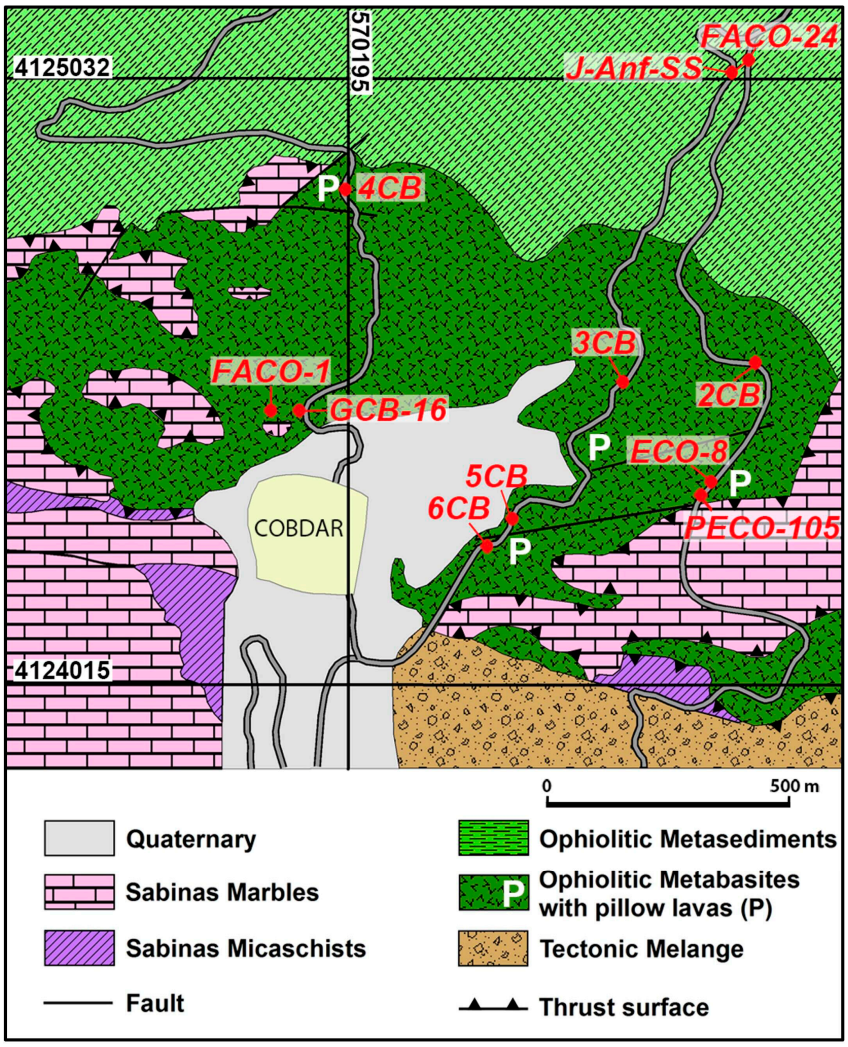


Figure 2. Geological sketch map of the Cóbdar ophiolite outcrop with the location of its dated rocks.

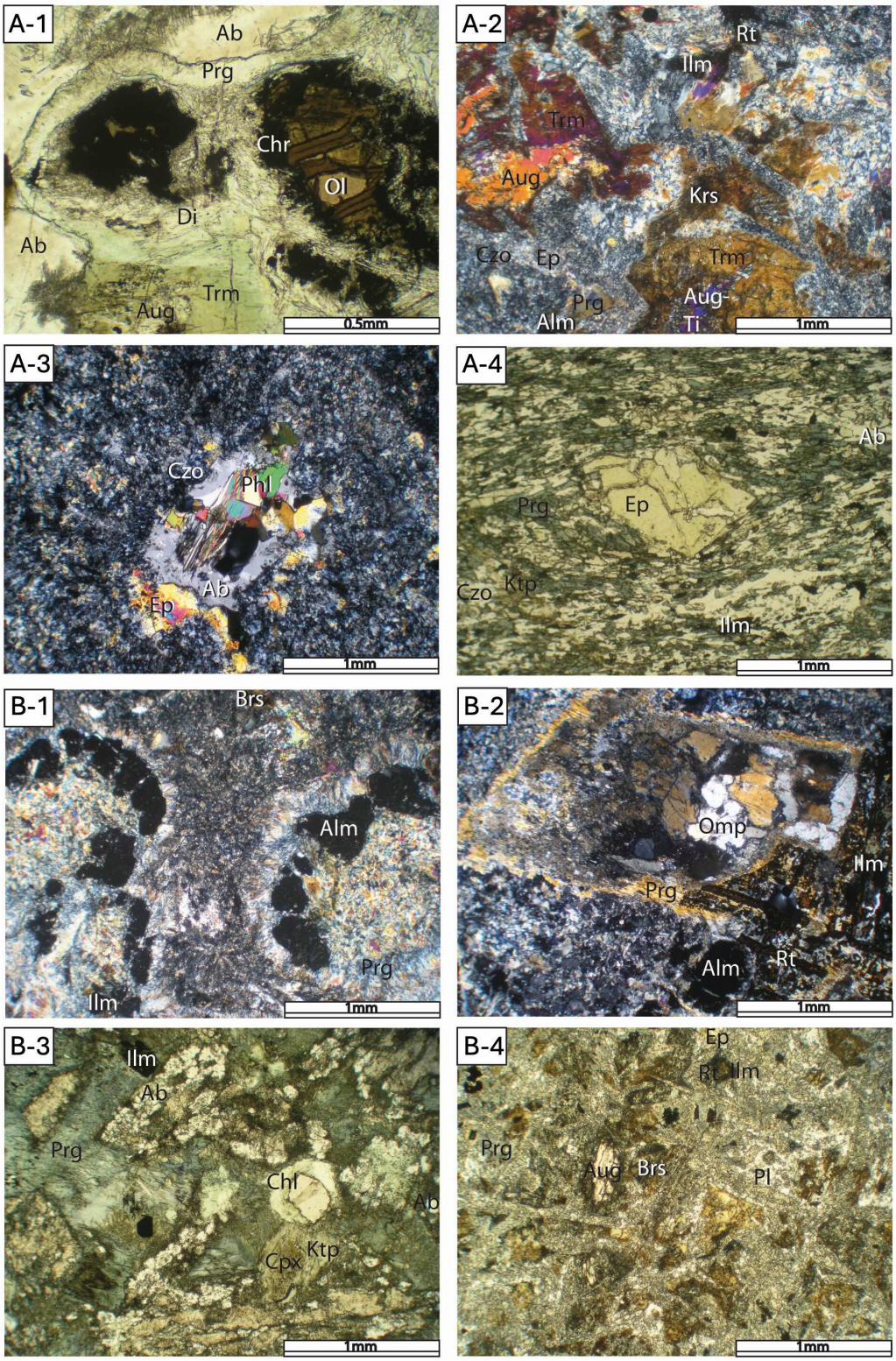


Figure 3. Microscopic photos of the main lithotypes forming the Cóbdar outcrop (**A-1**–**A-4**) and Algarrobo outcrop (**B-1**–**B-4**). Petrological characteristics are shown in Table 1.

Some complementary photos showing the good preservation of the flow and pillow structures of this outcrop can be seen in previous works (see Figure 3 of Ref. [3]). The brown color of oceanic floor minerals (kaersutitic amphibole, phlogopite, brown olivine with magnetite exsolutions) is also shown in this figure, which are locally preserved in some gabbros and basalts from Cóbdar that were less affected by the later orogenic metamorphism, as can be seen in Figure 3A-1 (sample 5CB) and also in previous works

(Figures 2 and 3 of Ref. [45]). These photos show igneous olivine being transformed into brown oceanic-floor olivine with magnetite–amphibole–pyroxene high-temperature exsolutions, and oceanic-floor brown amphibole aggregates surrounding vesicles and filling fissures in Cóbdar basalts [45].

Table 1. Petrology of the dated rocks from the Cóbdar (A) and Algarrobo (B) outcrops, indicating also the absolute age of these rocks, obtained by U/Pb with SHRIMP, and the number of zircons used in each Jurassic dating, together with the number of xenogenic pre-Jurassic zircons also dated from some of these Jurassic rocks.

(A) Cóbdar							
Sample	**Igneous lithotype**	**Metamorphic Rock Type**	**Igneous mineral relics**	**Ocean-floor minerals**	**HP minerals**	**LP minerals**	**Micro photos**
5CB (186.9 Ma.) 14 Zr Jur+1recr.	Ol-Px Gabbro	Amphib.-Eclogite	Ilm, La, Aug	Phlog, Krs	Alm, Omph, Rt	Ab, Ep, Chl, Czo, ClAlMg-Tar, Brs, Mg-Hbl, ClAl-Prg	
2CB (185.3 Ma.) 19 Zr Jur+1recr.	cum.Ol Gabbro	coronitic Ol-metagabbro	Ol(Criso), ClPx(Di-Aug), Ilm, La	br.Amph, Phl, Ap, Prg	Alm, Rt	vaz. Amph, Tr	A-1
3CB (184.3 Ma.) 8 Zr Jur	Px-Gabbro	Amphib.-Eclogite	Ilm, Ti-Aug		Omph, Alm, Rt, b-gr.Amph	Ep, Chl, Czo, Ab	A-2
6CB (176,2 Ma.) 2 Zr Jur	Porphyric Basalt	Ap-Ep Amphibolite	La, Cpx, Ilm	Phl, Ab	Czo, Ab, Omph, Rt	gr. Amph, Carb, Ab, Ed	A-3
FACO-24 (173.8 Ma) 3 Zr Jur./1Zr pre-Jur	Basaltic sill	Ab-Ep Amphibolite	Ilm		Ktp, Prg, Czo, Rt	Ep, Ab, Ms, Carb, Chl	A-4
(B) Algarrobo							
Sample	**Igneous lithotype**	**Metamorphic Rock Type**	**Igneous mineral relics**	**Ocean-floor minerals**	**HP minerals**	**LP minerals**	**Micro photos**
VS-2 (184.3 Ma.) 7 Zr Jur./ 12 pre-Jur	Ol-Px Gabbro	Amphib.-eclogite	Ilm		Omph, Alm, Rt, Czo	gr. Amph, Ms, Czo, Ab	B-1
P1-13 (182.6 Ma.) 14 Zr Jur+1 recr./ 5 pre-Jur	Ol Gabbro	Amphib.-Coronitic eclogite	Ilm, La	Tlc, ClFe-Prg	Alm, Rt, Czo	Brs, Prg, Ep	B-2
P1-62 (181.2 Ma.) 11 Zr Jur+54 recr./ 1 Zr pre-Jur	PxFe Dolerite	Amphib.-Omphacitite	Ilm		Omph, Rt, Gln, Alm	Prg, Ktp, Ab, Ep	B-3
P1-11 (179.6 Ma.) 13 Zr Jur/ 8 pre-Jur	Px Basalt	Amphib.-basalt	Ti-Aug, Ilm	br. Amph, Mg-Hs	bl-gr. Amph, Rt, Czo	Act, Carb, Chl, Tr, Mg-Hbl	B-4
P1-19 (177 Ma.) 1 Zr Jur/ 23 pre-Jur	Px Gabbro	Amphib.-Eclogite	Ti-Aug, La, Ilm		Omph, Alm, Rt	Prg, Czo, Ab	

The mineralogical composition of the dated metaigneous rocks from the Cóbdar and Algarrobo outcrops is shown in Table 1. This table also shows the successive mineralogical transformations during the different metamorphic stages that affected, more or less pervasively, each one of the basic rocks.

Table 1 also shows the number of Jurassic zircons used in the dating of each one of these (meta)gabbros, dolerite dikes, and basalts. These Jurassic zircons may coexist in the same sample with occasional xenogenic pre-Jurassic zircons in rare samples from Cóbdar (Table 2), or be more or less abundant than the pre-Jurassic zircons in the Algarrobo outcrop (Table 3). The petrological and geochemical study of these outcrops has been published

elsewhere (Ref. [3] and references therein). A dataset with the chemical composition of representative samples of Betic ophiolites from all sites mentioned in the text has been included as Supplementary Material (Table S1).

Table 2. Chemical composition of dated rocks from Cóbdar, also showing the number of zircons used in each Jurassic dating, together with the number of xenogenic pre-Jurassic zircons also dated from some of these Jurassic rocks.

Sample	**FACO-24**	**2CB**	**3CB**	**5CB**	**6CB**
Lithotype	**Basaltic Sill**	**Ol Gabbro**	**Px Gabbro**	**Px Gabbro**	**Porph. Basalt**
SiO_2 (%)	49.26	46.60	48.17	47.48	47.28
TiO_2	2.65	1.62	1.84	1.69	1.18
Al_2O_3	12.61	15.01	18.14	16.84	21.04
Fe_2O_3	9.88	10.80	9.21	8.65	7.78
MnO	0.06	0.17	0.15	0.16	0.08
MgO	1.07	12.11	4.92	9.65	3.75
CaO	11.88	8.38	9.90	8.71	11.65
Na_2O	6.79	2.52	3.51	3.03	3.42
K_2O	0.06	0.62	0.77	0.82	1.05
P_2O_5	0.67	0.22	0.32	0.30	0.25
LOI	4.87	0.93	2.14	1.83	1.92
Total	99.80	98.98	99.07	99.16	99.40
Rb (ppm)	0.8	6.2	11.0	7.8	20.3
Sr	199	280	363	449	825
Ba	4	88	55	153	75
Sc	34	25	28	27	18
V	306	182	186	188	151
Cr	60	621	173	340	135
Co	83	97	66	65	71
Ni	44	377	65	206	55
Cu	36	85	7	38	14
Zn	67	90	41	88	20
Y	50	21	25	23	20
Nb	12.7	10.7	5.3	7.6	6.8
Ta	1.10	0.98	0.66	0.80	0.59
Zr	11	93	147	41	43
U	0.44	0.25	0.28	0.32	0.36
Th	0.78	0.70	0.90	1.23	0.67
La (ppm)	18.57	8.39	11.01	12.12	10.51
Ce	39.29	19.73	24.79	27.82	23.27
Pr	6.02	2.68	3.52	3.79	3.11
Nd	27.63	12.31	16.39	16.53	13.69
Sm	7.31	3.50	4.41	4.16	3.45
Eu	2.38	1.14	1.37	1.30	1.33
Gd	8.06	3.61	4.34	3.85	3.58
Tb	1.26	0.60	0.72	0.60	0.60
Dy	8.38	3.85	4.53	4.13	3.65
Ho	1.76	0.79	0.96	0.93	0.78
Er	4.60	2.13	2.41	2.30	2.01
Tm	0.63	0.33	0.35	0.33	0.31
Yb	3.91	1.93	2.05	2.00	1.73
Lu	0.53	0.27	0.27	0.27	0.25
87Rb/86Sr	0.0121	0.0637	0.0880	0.0501	0.0710
87Sr/86Sr	0.704284	0.703156	0.704233	0.703240	0.704680
Error	0.003	0.002	0.003	0.002	0.002
147Sm/144Nd	0.160000	0.171900	0.162600	0.152200	0.152400
143Sm/144Nd	0.512912	0.513026	0.513023	0.513023	0.513066
Error	0.002	0.002	0.002	0.002	0.002
U/Pb age (Ma)	173.8	185.3	184.3	186.9	176.2
Jur. Zrs	3	19	8	14	2
Pre-Jur. Zrs	1				

Table 3. Chemical composition of dated rocks from Algarrobo, also showing the number of zircons used in each Jurassic dating, together with the number of xenogenic pre-Jurassic zircons also dated from some of these Jurassic rocks.

Sample	**P1-11**	**P1-13**	**P1-19**	**P1-62**	**VS-2**
Lithotype	**Px Basalt**	**Ol Gabbro**	**Px Gabbro**	**Px-Fe Gabbro**	**Ol-Px Gabbro**
SiO_2 (%)	49.08	47.52	50.58	50.72	47.53
TiO_2	1.62	0.86	1.69	2.24	0.98
Al_2O_3	16.88	17.83	16.22	14.99	16.08
Fe_2O_3	9.68	11.81	11.91	13.21	12.03
MnO	0.12	0.18	0.14	0.14	0.14
MgO	7.59	8.33	5.79	4.60	8.21
CaO	8.31	7.96	7.96	7.42	9.80
Na_2O	3.84	2.94	3.67	4.28	2.99
K_2O	0.59	0.17	0.23	0.23	0.25
P_2O_5	0.25	0.08	0.14	0.19	0.08
LOI	1.88	2.16	1.53	1.28	1.82
Total	99.84	99.84	99.86	99.30	99.91
Rb (ppm)	10.7	8.6	3.3	1.5	5.1
Sr	511	198	246	417	152
Ba	130	135	21	30	11
Sc	22	33	47	28	49
V	217	190	266	296	206
Cr	396	199	318	175	366
Co	29	49	31	25	38
Ni	117	141	35	27	99
Cu	47	93	52	16	42
Zn	67	89	71	60	47
Y	20	25	31	34	29
Nb	19.1	2.2	3.8	14.2	2.7
Ta	1.41	0.60	0.34	1.05	0.27
Zr	56	18	23	5	9
U	0.42	0.10	0.13	0.52	0.10
Th	1.09	0.20	0.49	0.92	0.10
La (ppm)	12.61	2.33	5.92	14.93	3.25
Ce	26.48	5.87	15.90	35.51	8.08
Pr	3.35	0.93	2.47	4.97	1.22
Nd	14.42	4.53	12.45	21.71	6.20
Sm	3.50	1.57	3.49	6.07	2.19
Eu	1.21	0.66	1.22	1.88	0.93
Gd	3.72	2.25	4.52	6.84	3.25
Tb	0.58	0.42	0.76	1.04	0.57
Dy	3.62	3.48	5.24	6.37	4.41
Ho	0.71	0.85	1.18	1.26	1.05
Er	1.83	2.51	3.27	3.31	3.00
Tm	0.26	0.41	0.45	0.49	0.46
Yb	1.56	2.55	2.68	2.77	3.06
Lu	0.22	0.36	0.36	0.38	0.47
87Rb/86Sr	0.0605	0.1260	0.0388	0.0104	0.0968
87Sr/86Sr	0.703897	0.704019	0.703576	0.705610	0.704723
Error	0.003	0.002	0.003	0.001	0.002
147Sm/144Nd	0.146600	0.208900	0.169300	0.169100	0.213900
143Sm/144Nd	0.512981	0.513000	0.512958	0.512953	0.512937
Error	0.002	0.002	0.002	0.003	0.007
U/Pb age (Ma)	179.6	182.6	177	180.8	184.3
Jur. Zrs	13	15	1	11	7
Pre-Jur. Zrs	8	5	23	1	12

The location of the dated rocks from the Algarrobo outcrop is shown in Figure 4. These metabasites mainly come from gabbroic outcrops with variable size, from several tens of meters (P1-13, P1-19) to up to more than 1 km (VS-2), which are formed by Ol and Px gabbros, represented by microphotographs B-1 and B-2 in Figure 3. These intrusive rock types are surrounded by doleritic and basaltic rocks with variable extension (P1-

11, P1-62), to which microphotos B-3 and B-4 in Figure 3 correspond. The labels of the mentioned dated samples have been simplified to be located on the map, together with other representative rocks lithologies, not containing enough zircons to be dated but that are very significant in terms of showing a more complete succession of the igneous sequence and their different degrees of metamorphic transformation into HP and/or LP assemblages, as shown in Table 1. Samples 4–16 correspond to a little volcanic outcrop that, despite the metamorphism affecting the surrounding rocks, locally preserves the volcanic texture and some aggregates of igneous olivine and acicular plagioclase in a perlitic matrix. Other, not dated rocks represented on the map are the following: ECV-6 and ECV-7, corresponding to the larger outcrop of eclogitized Ol-Px gabbros, such as the VS-8, which forms a dyke several decimeters thick of intrusive dolerite in the lower part of the meta-sedimentary sequence, and finally, VE-7 and VN-10, forming basaltic amphibolitized sills interlayered into the meta-sediments, which are very well represented in the eastern part of this outcrop.

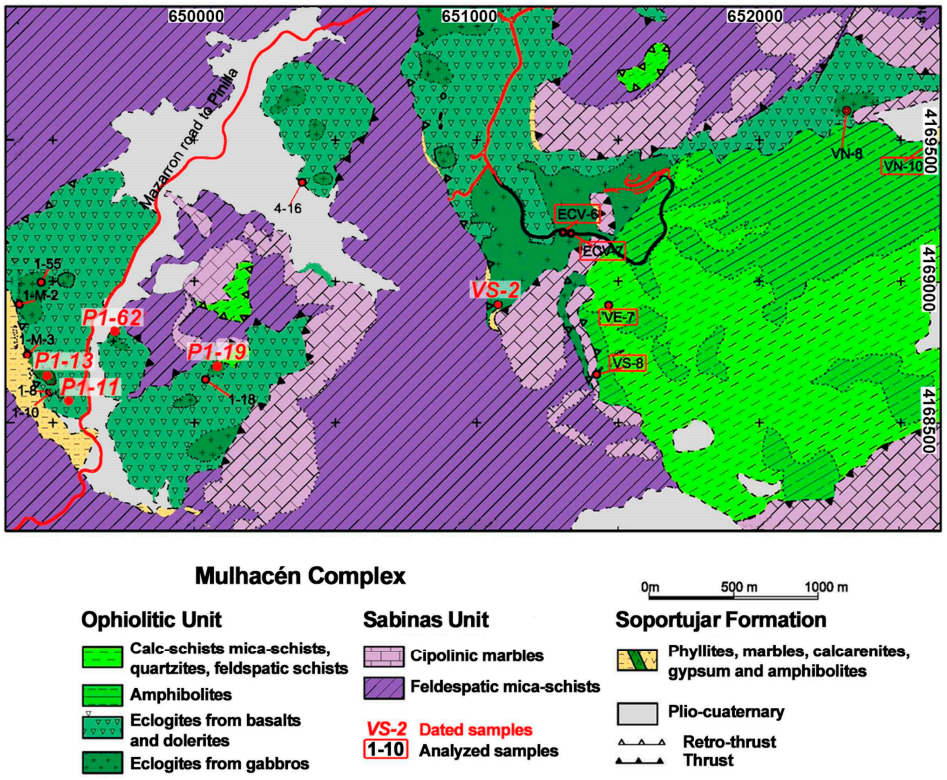


Figure 4. Geological sketch map of the Algarrobo ophiolite outcrop with the location of its dated rocks.

4. Geochemistry of the Betic Ophiolites

The chemical composition of the different rock types plotted on the maps of Figures 2 and 4 is shown in Tables 2 and 3 (dated rocks) and in Tables S2 and S3 (non-dated rocks) of the Supplementary Materials. Analytical techniques and other relevant information [46–53] are also provided in the Supplementary Materials.

4.1. Chemical Composition of the Betic Ophiolites and Their Tectonic Setting

The chemical composition of the Betic ophiolites is represented in the discriminant diagrams for the tectonic setting of Figure 5A–C, including previously published samples from the Lugros and Almirez outcrops (Ref. [3] and references therein). Chemical information from all published samples of the Betic ophiolites has been included in Table S1 and Figure S1 of the Supplementary Materials.

In Figure 5A–C we compare in the tectonic discriminant diagrams the four main outcrops of the Betic ophiolites, while in Figure 5D we only represent the REE pattern of the five dated metabasites from the Cóbdar and Algarrobo outcrops in order to elucidate the temporal evolution of the magmatism in these two outcrops.

Figure 5A highlights the subduction-unrelated setting and MORB chemical character of the Betic ophiolites, such as the progressive and differential enrichment from N-MORB to E-MORB, which is more notable in the Algarrobo than in the Cóbdar outcrop. Median values from Ref. [56] for normal MORBs (+N) and enriched MORBs (+E) are also shown for comparison. In Figure 5B we have plotted the chondrite-normalized $(Ce/Yb)_N$ vs. $(Dy/Yb)_N$ of Refs. [52,54] to discriminate a sub-type of N-MORBs showing a garnet signature (G-MORB), which is generated in Alpine-type continental rifts and OCTZs (Oceanic–Continental Transitional Zones), from typical N-MORBs in some ophiolites of the Western Tethys. The Betic ophiolites represented in Figure 5A,B are not plotted only in the N-MORB and probable G-MORB fields but are also extended mainly along the E-MORB field, because they are characterized by higher values of $(Ce/Yb)_N$ vs. $(Dy/Yb)_N$ ratios than those represented in Ref. [54]. These comparisons suggest that the Betic ophiolites derived from the westernmost end of the Neotethys mostly originated in an oceanic floor tectonic setting, as corresponds to their marked E-MORB character, and not in an OCTZ or continental rift tectonic setting that characterizes other ophiolites derived from the Western Tethys [52].

Sr and Nd isotope ratios for the Cóbdar and Algarrobo ophiolites, together with those from Lugros and Almirez published in Ref. [7], are shown in Figure 5C. Values for the basic rocks of the Betic ophiolites are similar and overlap those from the Internal Ligurides [57] and Platta Nappe basalts [58], interpreted by these authors as deriving from a MORB-type mantle source. These isotopic ratios and those corresponding to ultramafic rocks from the Almirez outcrop are also similar to those reported by Ref. [59] for peridotites and basalts from the Mid-Atlantic Ridge at the Vema Fracture Zone. Metagabbros from the Cóbdar, Algarrobo, and Lugros outcrops have an Nd isotope signature similar to the MORB from present-day slow and ultra-slow ridges such as the Mid-Atlantic Ridge and South West Indian Ridge. However, metabasalts from the same outcrops, mainly the Almirez rodingitized dykes and their meta-ultramafic host rocks, present a higher Sr isotope signature and some decrease in the Nd isotope signature. A similar variation in Sr isotope signature may be explained by extreme oceanic-floor metasomatism triggered by water/rock interaction with Jurassic seawater, with $^{87}Sr/^{86}Sr$ varying from 0.7072 to 0.7075 according to Ref. [60]. Similarly, abyssal peridotites from current oceanic fracture zones (plotted in Figure 5C) also show an increase in $^{87}Sr/^{86}Sr$ isotope values, due to contamination by present-day seawater, with $^{87}Sr/^{86}Sr = 0.7092$, together a strong decrease in $^{143}Nd/^{144}Nd$ isotope ratios, according to Ref. [55].

Finally, in Figure 5D we only represent the REE values of the ten dated metabasites from the Cóbdar and Algarrobo outcrops, with green and violet numbers, respectively, with the aim of elucidating the temporal evolution of the magmatism in each of these two outcrops in relation to the depth of the mantle source and chemical evolution of their respective magmas during the accretion time of the oceanic floor. In the upper part of this figure we have included the labels corresponding to the five dated rocks from the Cóbdar and Algarrobo outcrops, such as their respective symbols in this figure, together with a number that indicates the decreasing order of their igneous zircon crystallization, from the oldest (1) to the youngest (5), corresponding to the age of the magmas originating in each one of the dated rocks. The absolute age of these ten rocks, together with the number of Jurassic zircons on which this radiometric dating is based, can be seen in Tables 1–3, according to the dating results presented in the next section. These REE patterns from the

Cóbdar and Algarrobo outcrops, together with the patterns of other Betic ophiolites (see Figure S1A,B), suggest a tectonic environment corresponding to the origin of an oceanic ridge, developed from the rifting of a continental margin (Figure S1C), which evolved up to a MOR type (Figure S1D). This latter tectonic environment is the most common type identified in the Betic ophiolites. Both types of environments are common in the subduction-unrelated ophiolites recognized by Ref. [61], and are also represented in Ref. [62]. The MORB setting has been indicated as characterizing the Betic ophiolites in the Phanerozoic ophiolites in the global distribution map of Ref. [63], following the data published in Ref. [7].

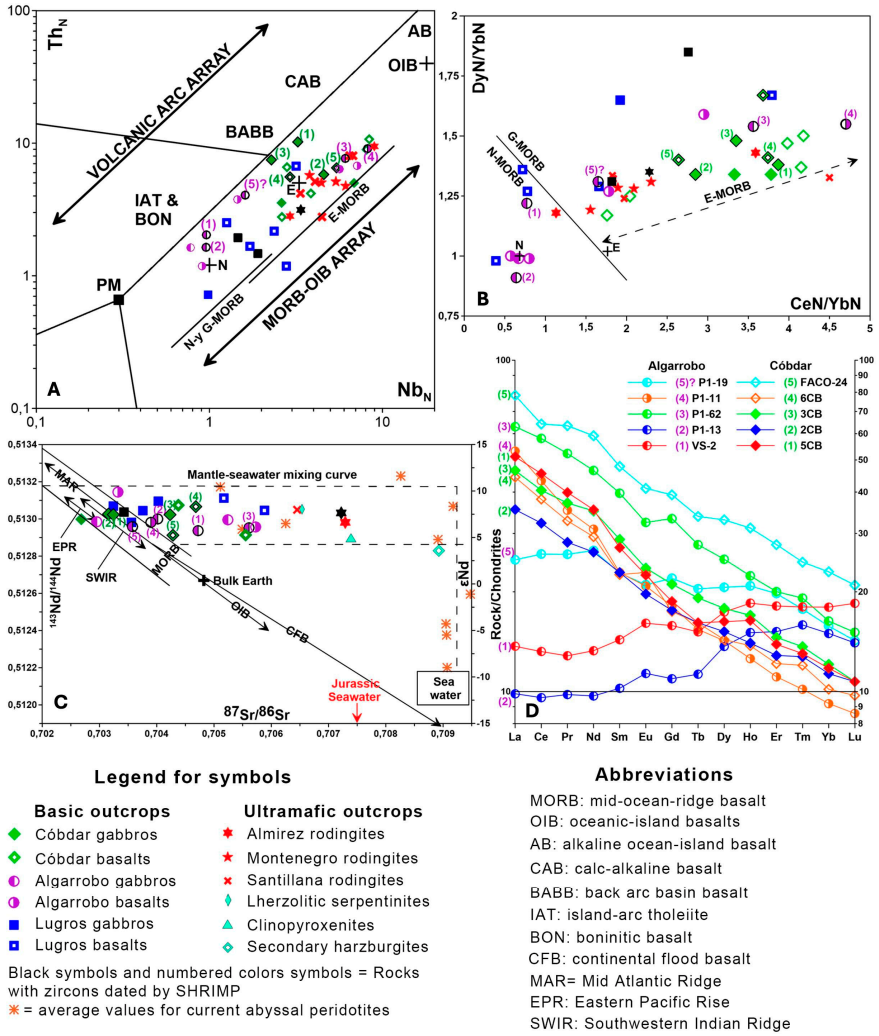


Figure 5. Discriminant diagrams for the tectonic setting of the Betic ophiolites. Representative basic and ultramafic rock compositions from the main Betic ophiolitic outcrops [3,7,25] have been plotted in the following diagrams: (**A**) NMORB-normalized Th_N vs. Nb_N [54]; (**B**) chondrite-normalized $(Dy/Yb)_N$ vs. $(Ce/Yb)_N$ [54]; (**C**) Sr vs. Nd isotopic ratios for basic and ultramafic rocks, compared with those in abyssal peridotites (data from Ref. [55]); (**D**) chondrite-normalized REE values for the different samples with zircons dated from the Cóbdar and Algarrobo outcrops. MORB and chondrite normalization values from Ref. [56]. Numbers (1) to (5) in parenthesis indicate the crystallization order, or successive magmatic levels, in the Cóbdar (green color) and Algarrobo (violet color) outcrops. Abbreviations: MORB: mid-ocean-ridge basalt, N-: normal type, E-: enriched type, G-: garnet-influenced type. OIB: oceanic-island basalt. AB: alkaline oceanic-island basalt. CAB: calc-alkaline basalt. BABB: back arc basin basalt. IAT: island-arc tholeiite. BON: boninitic basalt. MAR = Mid-Atlantic Ridge. EPR: Eastern Pacific Rise. SWIR: Southwestern Indian Ridge. CFB: continental flood basalt.

4.2. Magmatic and Temporal Relationships Among the Dated Rocks from Cóbdar and Algarrobo Compared with Those from Lugros and Almirez

In the Cóbdar outcrop the five dated rocks present REE patterns normalized to chondrites corresponding to an E-MORB character (Figure 5D). The three older rocks (5CB, 2CB, and 3CB), whose ages, respectively, are 186.9, 185.3, and 184.3 Ma (Table 1), come from different gabbroic layers, as can be seen in the map of Figure 2, but the three are formed by Ol-Px gabbros, partly transformed into eclogites and amphibolites (Table 1 and Figure 3A-1,A-2). The magmas that led to these gabbros present similar Yb_N contents, higher than a value of 10, indicating a magma source deriving from a spinel-bearing mantle layer (Figure 5D). The dated rock following next in time (6CB) corresponds to a meta-basalt, with a probable age of about 176 Ma (Table 1), overlayered by a non-dated pillow lava level. The Yb_N value of sample 6CB, close to 10, suggests the provenance of the magma from which it originated as being from the limit of a spinel with a garnet-bearing mantle layer. Finally, the FACO-24 and JAnfSS rocks (two similar samples of the same uppermost layer), with zircons dated as 173.8 Ma (Table 1), present a higher Yb_N value (higher than 20), which would indicate a notable elevation of the source of the magmas during the final volcanic stage. This late volcanic episode led to thin basaltic layers and sills, which were interlayered between the lower metasediments of the cover of this ophiolite outcrop.

The Algarrobo rocks present a higher variety of REE patterns from magmas of an N-MORB to E-MORB character derived from a spinel-bearing mantle layer, with Yb_N comprising values of between 15 and 18 for the older gabbroic and doleritic rocks, VS-2, P1-13, and P1-62, whose absolute ages are 184.3, 182.6, and 180.8 Ma (Table 1 and Figure 3B-1–B-3). The subsequent magmatic level in this outcrop, represented by sample P1-11, of 179.6 Ma, corresponds to a final volcanic activity leading to basalts with scarce pillow- lavas that underwent a clear oceanic-floor metamorphism (Figure 3B-4). The magma that created these basalts, with $Yb_N < 10$, would derive from a garnet-bearing mantle source, clearly deeper than the source of the magmas creating the previously formed gabbros in this outcrop (Figure 5D). A similar increase in the depth of the magma source, from the gabbro to the basalt development in the Algarrobo outcrop, seems to have taken place also in the Cóbdar outcrop, between the magmas leading to the gabbro layers (5CB and 2CB) and the first pillowed basaltic layer (6CB), which also presents an LREE-enriched pattern, similar to the P1-11 basaltic layer (Figure 5D). The difference in magmatic evolution between these two outcrops is that the magmatic source depth in the Cóbdar outcrop clearly decreased at the end of the volcanic stage (sample FACO-24), which coexisted with the beginning of the sedimentary sequence development, much more so than the volcanic source depth at the Algarrobo outcrop (sample P1-11), as is clearly shown by the different Yb_N values between these two samples in Figure 5D.

Gabbros and basalts from the Lugros outcrop, represented in Figure 5A–C as full and open blue squares, respectively, extend from N- to E-MORB, similarly to those from the Algarrobo outcrop. Only two eclogitized gabbros from the Lugros outcrop, ELUG-61 and ELUG-63, whose zircons were dated by SHRIMP as 185 and 187 Ma, respectively [7,64], are represented as black and full blue squares, respectively (Figrues 5A–C and S1A). The REE-normalized patterns of the more significant Lugros outcrop rocks (Figure S1A) are plotted, with full squares indicating those deriving from gabbros and open squares indicating those deriving from basalts (see the petrographic description of these samples in Refs. [7,64]). ELUG-61 and ELUG-63 present a predominant E-MORB character, with lower HREE values in the gabbroic rocks, which are derived from a garnet-mantle field deeper than the basalts (such as ELUG-Pr), which mainly would come from a spinel-mantle field. Nevertheless, there are some exceptions, like that represented by the lower pillow lava level containing

Ol phenocrysts such as ELUG-17, which present an N-MORB character close to G-MORB (Figures 5B and S1A, with data from Ref. [65]).

In Figure 5A–C, 12 chemical analyses of rodingites forming decimetric to metric boudinaged dykes of basic rocks intruding in the serpentinized ultramafic outcrops of Almirez, Santillana, and Montenegro are plotted (see Figure 1 and Table S1). The petrological and geochemical studies of these rodingites, such as their genetic relationships with the first oceanic serpentinization process undergone together with their host ultramafic rocks, were previously published in Refs. [66,67]. Meanwhile, the radiometric U-Pb dating of their zircons from the Almirez outcrop was published as 184 Ma in Ref. [7]. The rodingites are represented in Figure 5A–C, with different symbols according to their outcrop of provenance, but all in red, with the exception of the dated sample ZL-57, which is represented in black. The REE patterns of a selection of these rodingitized metabasite dykes from the Almirez, Santillana, and Montenegro outcrops are shown in Figure S1B of Supplementary Materials. The REE patterns of the selected rodingites in this figure show that these rocks mainly derive from an E-MORB-type magma, with provenance from a spinel-bearing mantle with Yb_N values higher than 10. These REE patterns are similar to those forming mainly the volcanic sequence in other Betic ophiolite outcrops (see Figures 5D and S1B), although they can be easily distinguished from the other Betic ophiolite metabasites by their higher CaO (11 to 27%) and lower Na_2O (0.1 to 6%) contents (Table S1 of the Supplementary Materials) compared to non-rodingitized metabasites, with an average CaO content of less than 10% and an Na_2O content close to or higher than 4%. These chemical differences originated from the rodingitization process of the basic dykes, which are intrusive in ultramafic rocks and took place mainly during the oceanic serpentinization of their host rocks (see the chemical evolution curve of rodingitization in Refs. [66–68]).

5. Zircon Study with SHRIMP

In this section, we will discuss the geochronology, morphology, and chemical composition of the zircons dated by U-Pb with SHRIMP from the Cóbdar and Algarrobo outcrops, and compare the results with those from the Lugros and Almirez outcrops that were previously published [7]. Analytical techniques are described in the Supplementary Materials.

5.1. SHRIMP U-Pb Data Results for Zircons from Cóbdar and Algarrobo

Figure 6 shows the Tera–Wasserburg diagrams [69], together with the probability density histograms, corresponding with the weighted mean $^{206}Pb/^{238}U$ ages calculated for the dated samples from the Cóbdar (Figure 6A) and Algarrobo outcrops (Figure 6B) using ISOPLOT/EX [49].

The igneous weighted mean ages in Figure 6A,B are mainly formed by the dating group close to the Concordia curve, while the scattered analyses, which are plotted above these curves, are probably related to later recrystallization processes. Tables S4–S8 of Supplementary Materials show the summary of the SHRIMP U-Pb results for zircons from samples 5CB, 2CB, 3CB, J-Anf-SS/Faco-24, and 6CB, respectively. At the foot of each table the number of zircon crystals on which the dating results are based is indicated, corresponding to each sample, such as other precisions about the calculation of the analytical data represented in the corresponding table.

The Tera–Wasserburg diagrams of samples 5CB, 2CB, 3CB, and J-Anf-SS/Faco-24 (Figure 6A) represent the calculated U-Pb average ages for each one of these Cóbdar samples, considered also the age of the different dated magmatic levels, ordered from the oldest (1° Cob) to the youngest (5° Cob). The first three samples correspond to metagabbros and the last one to the upper volcanic layer, which also contains some sills interlayered

into the overlying sedimentary sequence, whose ages consequently correspond to the final stage of the oceanic floor magmatism.

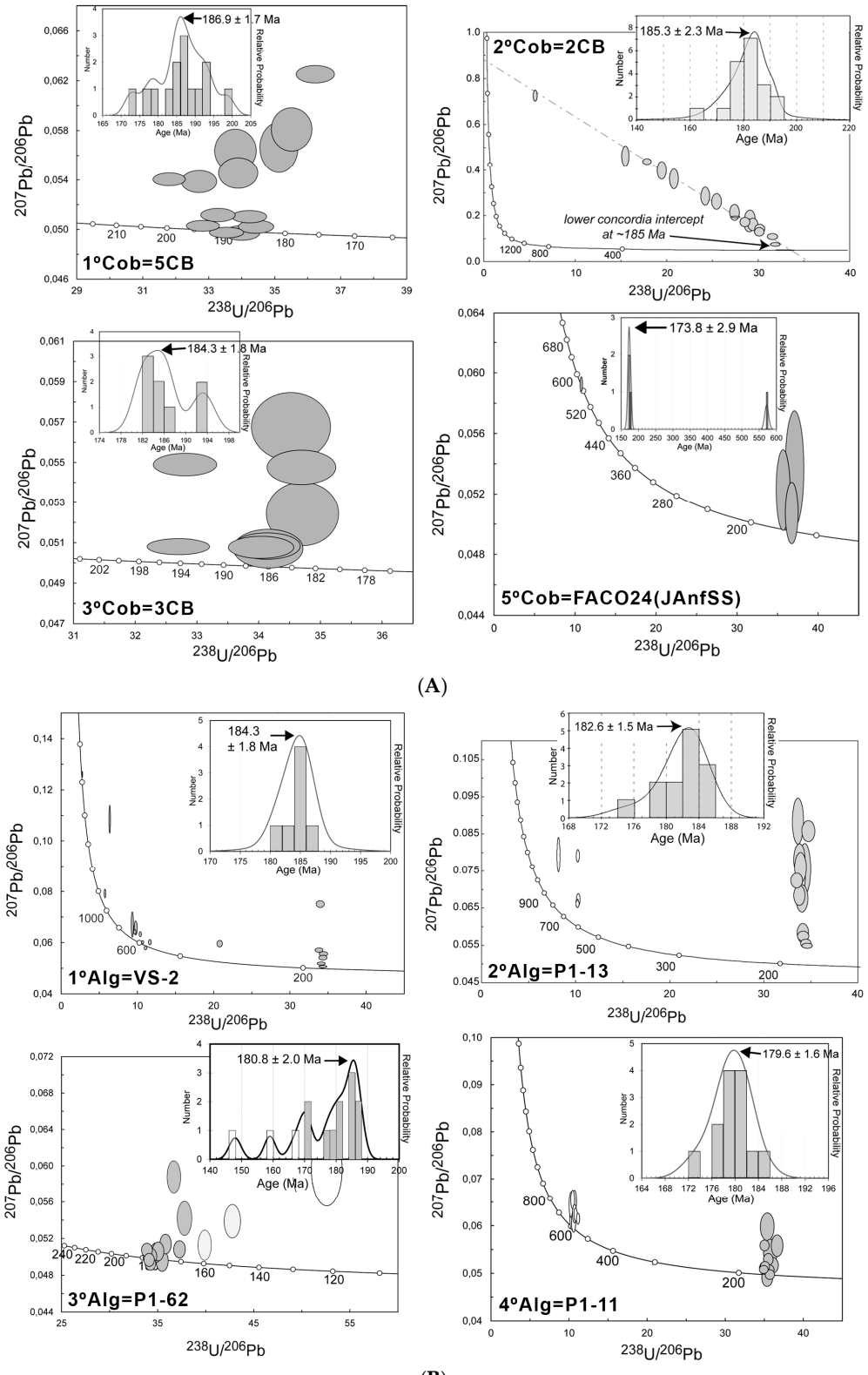


Figure 6. (**A**). Tera–Wasserburg diagrams together with probability density histograms showing the calculated weighted mean U-Pb ages for the Cóbdar samples. (**B**). Tera–Wasserburg diagrams together with probability density histograms showing the calculated weighted mean U-Pb ages for the Algarrobo samples.

In sample 5CB, 14 SHRIMP U-Pb analyses were obtained, yielding a $^{206}Pb/^{238}U$ weighted average main grouping of 186.9 ± 1.7 Ma. One recrystallized zircon, type III (in blue color in Table S4), is interpreted as corresponding to alpine orogenic metamorphism, with an age of 28.1 Ma. These U-Pb dating analyses were performed on subhedral and euhedral crystals with weak oscillatory zoned patterns. This zoning is shown in cathodoluminiscence (CL) photos in Figure S2 (upper panel), by crystals 1 and 2 of group 1° (5CB = 1°-1 and 1°-2). In sample 2CB, 16 zircons were dated, with 19 analyses, of which 18 preserve igneous compositions, yielding a U-Pb mean age of 185.3 ± 2.3 Ma, and one of them corresponds to a recrystallized crystal probably under ocean-floor conditions of type II (in green in Table S5), with an age of 161.7 Ma. These dating analyses were performed on subhedral crystals with a similar oscillatory zoned pattern as the previous sample and some altered areas that may be present in some crystals of group 2° (Figure S2). In sample 3CB, eight zircons were dated, yielding an igneous mean U-Pb age of 184.3 ± 1.8 Ma (Figure 6A) on subhedral crystals, with some altered rims, such as those representing group 3° in Figure S2. Finally, in the FACO-24/J-Anf-SS sample, four zircon crystals were dated. Three of them yielded a mean U-Pb age of 173.8 ± 2.9 Ma (Figure 6A), representing the magmatic group 5° in Figure S2, and another crystal, Precambrian in age (572 Ma), which is also presented in Table S7. Between the magmatic levels represented in Figure 6A (from magmatic levels 3° and 5°) there exists in this outcrop another, well-developed volcanic level containing pillow lavas (Figure 2), to which the Zr10-6CB sample corresponds, with only two zircons dated by SHRIMP, and whose U-Pb ages are 169.9 + 1.7 Ma and 182.4 + 2.1 Ma, representing an average age of about 176 Ma (Table S8).

From the Cóbdar outcrop another four zircon crystals were dated with Precambrian ages, from 579 to 638 Ma in samples FACO-1 and GCB-16, forming part of the basal magmatic level in this outcrop (Figure 2). These data can be seen in Table S9, and the morphologic and CL images, characterized by euhedral crystals with marked oscillatory zoning, are shown in Figure S3. These four crystals were the only zircons crystals that could be separated from about 20 kg of powdered metabasite, coming from a basal magmatic level, similar to sample 5CB, dated as forming part of group 1° by the dating of their Jurassic zircons (Figure 6A and Table S4). Locally, this basal metabasite contains relics of quiastolite crystals transformed into corundum and spinel [70,71], but they do not contain datable zircon crystals.

Figure 6B, represents the Tera–Wasserburg diagrams, together with the probability density histograms and the weighted mean $^{206}Pb/^{238}U$ ages, calculated for the dated samples from the Algarrobo outcrop, corresponding to the samples VS-2, P1-13, P1-62, and P1-11. The different U-Pb dating represented in the composed diagrams of Figure 6B are also shown in more detail in Tables S10–S13. These dating analyses correspond to the four magmatic levels, which are ordered from 1° to 4°.

In sample VS-2, seven subhedral Jurassic zircons were dated, with an average U-Pb dating of 184.3 ± 1.8 Ma, representing the first magmatic level in the Algarrobo outcrop (Figure 6B), together with 12 pre-Jurassic zircons, composed of 11 Precambrian euhedral crystals, from 530 to 1975 Ma, one of which is an Upper Carboniferous with an age of 300 Ma (Table S10 and Figure S3). Figure S3, when compared with Figure S2, shows the notable morphological differences existing between the Jurassic and the coexisting pre-Jurassic zircons of the same sample, such as the total absence of overgrowth of pre-Jurassic zircons by Jurassic crystal rims in this outcrop. This fact is also corroborated by the zircons of other dated samples in the Betic ophiolites, indicating the xenogenic character of the Pre-Jurassic, mainly Precambrian, zircons, with respect to their hosting Jurassic magmas in these ophiolites. Moreover, the total absence of overgrowth of Jurassic zircon crystals taking as cores some pre-Jurassic zircons can be seen in the representative CL images of

the sectioned grains. Fifteen Jurassic zircon crystals were dated in sample P1-13, yielding an average U-Pb age of 182.6 ± 1.5 Ma, which would correspond to magmatic level 2° in the Algarrobo outcrop. The Jurassic zircons in this sample are euhedral to subhedral and present some corroded and recrystallized rims, with an age of about 152 Ma, which must have originated under ocean-floor conditions (Type II in Table S11). In this sample, five Precambrian zircons were also dated, from 590 to 736 Ma, with similar CL and morphology to those of similar age represented in Figure S3 and different to the Jurassic zircons in this sample (Figures S2 and S4). For sample P1-62, the radiometric dating presents a main average igneous age of 180.8 ± 2.0 Ma for twelve euhedral zircon crystals (Figure 6B and Table S12), and several recrystallization ages interpreted as corresponding to oceanic floor alteration processes (159–148 Ma, noted as type II in Table S12) and to different orogenic metamorphic processes (about 120 and 28 Ma, type III in this table), which were also previously identified in zircons from other Betic ophiolitic outcrops [3,7]. The morphology and the CL aspect of the preserved igneous areas and those of the recrystallized ones can be seen in Figure S2 for crystals 1 and 2 of sample P1-62, which correspond to magmatic level 3° in the Algarrobo outcrop. In this rock, only one Precambrian zircon was found and dated as 937.5 ± 10.9 Ma (Table S12). Finally, from sample P1-11, 20 zircon crystals were dated, of which 13 are Jurassic in age, with a mean radiometric U-Pb dating of 179.6 ± 1.6 Ma (Figure 6B and Table S13), representing magmatic level 4° in this outcrop. The remaining eight zircons are Precambrian, with radiometric ages of between 552 and 595 Ma (Figures S3 and S4). Some of the Jurassic crystals present oscillatory zoning at their preserved igneous borders, as shown in Figure S2 by spot 16.1 of crystal 4°-2, with an age of 184.5 Ma, which also presents some irregular areas with higher luminescence and lower age, such as spot 16.2 with an age of 178 Ma, very probably due to a post-magmatic recrystallization process.

In Figure 6B, the Tera–Wasserburg diagrams VS-2, P1-13, P1-62, and P1-11 represent, respectively, the different magmatic levels average ages, ordered from the oldest (1° Alg) to the youngest (4° Alg). The first three levels correspond to metagabbros and the last one to a metabasalt (Table 1). The main difference between these Tera–Wasserburg diagrams in the Algarrobo samples and those corresponding to Cóbdar (Figure 6A) is the presence in some of the Algarrobo outcrop levels of abundant pre-Jurassic zircons, together with those Jurassic in age, used to discriminate the existence of the four levels of Jurassic magmatism. These pre-Jurassic zircons are mostly Precambrian in age, as can be seen along and above the concordia curves in the diagrams, corresponding to Jurassic magmatic levels 1°, 2°, 3°, and 4° Alg (Figure 6B), and with more precision in the different enclosed Tables S10–S14, in which, for samples VS-2, P1-13, P1-62, and P1-11, the SHRIMP U-Pb pre-Jurassic ages are represented in red, while those corresponding to Jurassic zircons are represented in black, and Jurassic zircons recrystallized by oceanic-floor metasomatism or orogenic metamorphism are represented in green or blue.

5.2. Geochemistry of the Jurassic and Locally Pre-Jurassic Zircons of the Betic Ophiolites

Selected U and Th compositions of Jurassic and pre-Jurassic zircons coexisting in some samples of the Betic ophiolites are plotted in Figure 7. Data for Cóbdar and Algarrobo are included in Tables S4–S14, while data for other Betic ophiolite outcrops, such as Lugros and Almirez, have been published elsewhere [3,7,64]. As mentioned before, Jurassic zircons coexisting with the pre-Jurassic ones are never found to be overgrowth of the older ones, indicating the xenogenic character of the pre-Jurassic (mainly Precambrian) zircons, with respect to their host Jurassic magmas. This is also in agreement with their chemical differences (Figure 7A–D). Moreover, this spatial relationship is similar to that

characterizing the coexistence of current and pre-Jurassic zircon crystals found in the dredged basic rocks along the MAR [72] represented in Figure 7E,F.

Cathodoluminiscence characteristics of each one of the dated zircon crystals mainly depend on their U and Th contents and Th/U ratios, with the zircon areas richer in U having a darker grey color (see the CL photos in Figures S2–S6, and the U-Th contents in Tables S4–S14).

Figure 7A shows the U vs. Th plot of 51 igneous zircons analyses from the Cóbdar outcrop, 48 of which correspond to Jurassic zircons and were represented as half full dots, with different colors according to the sample and magmatic level of provenance, while the other five correspond to pre-Jurassic zircons and have been represented as full-rhombs, with the color indicating their provenance level, as shown in the inset. The numbers represented in this figure correspond to some of the dated spots of the main igneous and recrystallized zircons, deriving from the different magmatic levels, whose CL aspect can be seen in Figure S2. The zircons from the Cóbdar outcrop, dated as Jurassic in age, present U and Th contents in accordance with these two trace element values in the corresponding whole rocks (Table 2).

Th/U ratios in Jurassic zircons, mainly in non-recrystallized igneous areas, are commonly higher than 1 (Tables S4–S14), attaining values higher than 7 in samples such as P1-11. Meanwhile, the pre-Jurassic zircons in all the Betic ophiolites analyzed present values of the Th/U ratio close to or less than 1. In recrystallized areas of Jurassic zircons, such as the one shown in spot 16.2 of sample P1-11 (Figure S2), the Th/U ratio decreases to 3.19 from a value of 7.24, which represents the igneous core of the same crystal (Table S13). This change in Th/U ratio is due to a strong loss of Th and U during the recrystallization process, which also increases the CL response of this area, changing the grey color of the igneous crystal (spot 16.1) for the white color in the recrystallized area (spot 16.2).

In some of these zircons, the cores and rims have also been dated, like in crystal 2 of sample 5CB (Figure S2), yielding two different ages: 179.4 Ma for the core (spot 15.2) and 172.7 Ma for the rim (spot 15.1). In Figure 7A, these two spots in the zircon crystal are united by an ascending arrow, indicating the increase in U and Th from 301 and 697 ppm to 453 and 3337 ppm, respectively, while Th/U ratio varies from 0.539 in the core to 2244 at the rim during the period of development of this crystal, which could be of about 6 Ma. A similar case of increase in U and Th contents from core to rim development are presented by crystal 2 of magmatic level 2° (2CB) in Figures 7A and S2, whose spot 8.2, with 179.5 Ma in the core, changes to spot 8.1 at the rim, with 174.8 Ma. Meanwhile, the U increases from 238 to 453 ppm, the Th from 697 to 3337 ppm, and the Th/U ratio from 2320 to 7366. Also shown in Figure 7A, a descending arrow joins spot 1.2 for the same sample (2CB), with U = 731 and Th = 4513 ppm, together with a rimming area in the same crystal (spot 1.1), represented as a red square. This area presents a lower U (97 ppm) and Th (347 ppm), and probably originated during an oceanic-floor recrystallization process, which also led to a decrease in the U-Pb dating age from 183.7 to 177.2 Ma (Table S5). Finally, spot 9.1 in sample 5CB, represented as a blue square, corresponds to a less common zircon crystal, with an age of 28.1 Ma, that contain U 7609 ppm, Th 11,959 ppm, and a Th/U of 1.57. The CL aspect of this zircon crystal is a very dark grey color due to its high U content, which is higher than any other analyzed crystal of the same sample. This zircon type must be interpreted as having originated during the alpine metamorphic event.

Figure 7A also represents, as full rhombs, the five Precambrian zircons found in the Cóbdar outcrop. Four of them, in green in this figure, derive from a basal level (FACO-1 and GCB-16) not containing dated Jurassic zircons, and their ages vary from 579 to 638 Ma (Table S9 and Figure S3). The other Precambrian zircon crystal, with an age of 571.7 Ma, represented as orange rhomb in Figure 7A, was found in the JAnf-SS sample of the upper

magmatic level (n° 5), and is characterized by Th and U values clearly higher than those of the three Jurassic zircons dated from the same sample, represented as orange half-full dots, indicating a xenogenic origin for this Precambrian zircon relative to the host magma from which the Jurassic zircons derive.

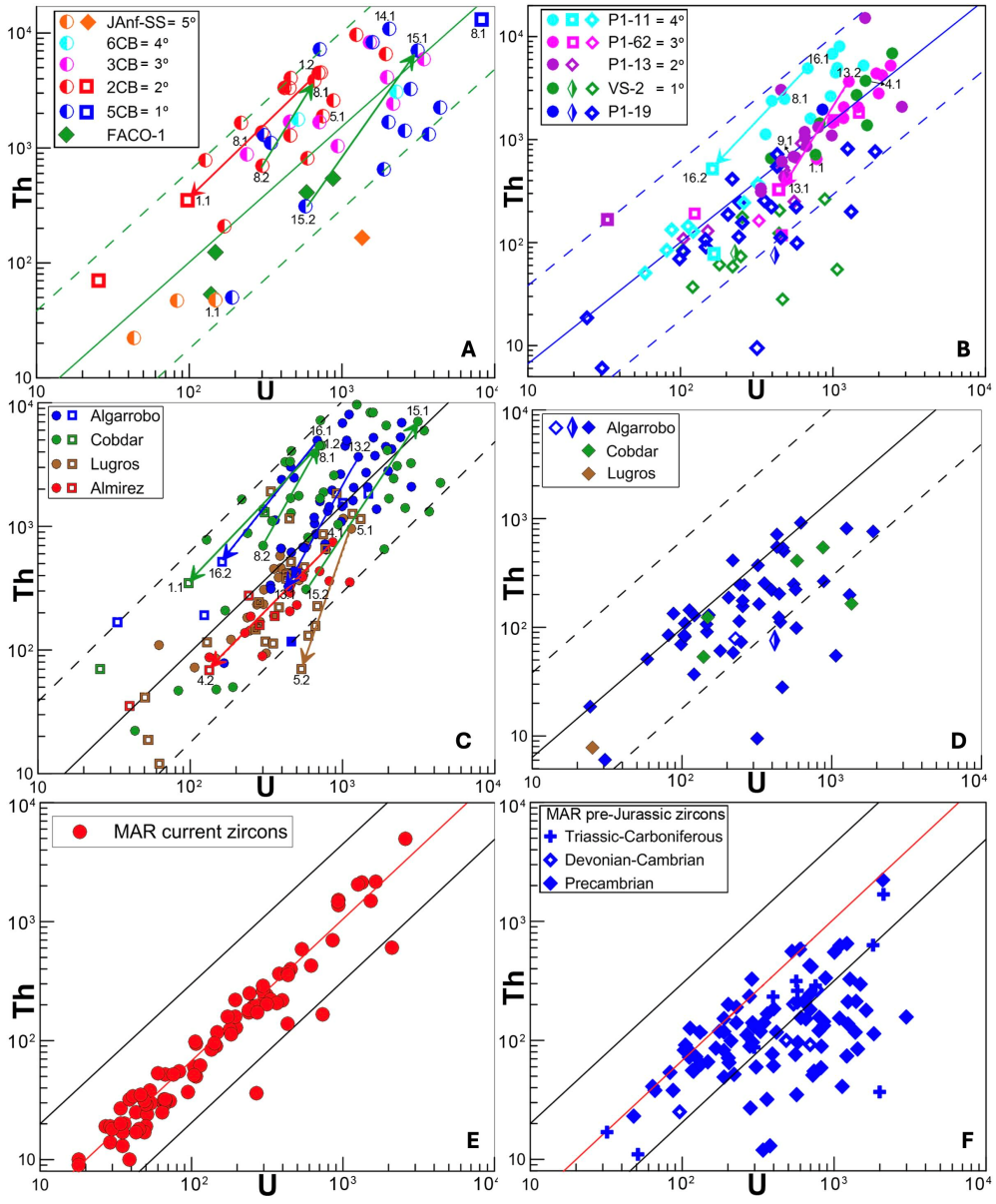


Figure 7. U-Th compositions of Jurassic and pre-Jurassic zircons coexisting in some samples of the Betic ophiolites (**A**–**D**) and comparison with current and Precambrian zircons dredged in the MAR (**E**,**F**). Meaning of the insets in the (**A**) Cóbdar and (**B**) Algarrobo outcrops: The round forms of the symbols correspond to igneous Jurassic zircons, the squares to Jurassic recrystallized crystals, and the rhombs to pre-Jurassic zircons. Numbers 1° to 4° or 5° indicate the successions of magmatic levels from bottom to top, to each one of which the name of a sample and the color of its symbol correspond. Meaning of the inset in (**C**), only for Jurassic zircons (round symbols) and recrystallized zircons (squares symbols), from the following outcrops and symbol colors: Algarrobo (blue), Cóbdar (green), Lugros (brown), and Almirez (red). (**D**) Only pre-Jurassic zircons, from outcrops with the same colors as in (**C**). (**E**) Round red symbols: current MAR zircons. (**F**) Pre-Jurassic MAR zircons, with three symbols whose ages are indicated in the inset of this figure.

Figure 7B shows the U vs. Th plot of 53 Jurassic zircons (represented as full dots and open squares), together with 48 pre-Jurassic zircons (open rhombs), from the different

samples of the Algarrobo outcrop. The Jurassic and pre-Jurassic zircons from the different samples are represented with different colors, as shown in the inset, which also indicates the name of the samples and the order number of the magmatic level corresponding to each one. In this figure, is easy to distinguish the higher values of Th and Th/U contents that the Jurassic zircons present with respect to those of the pre-Jurassic age in each one of these samples, from VS-2 to P1-11, indicating different genetic conditions between these two zircon types. In fact, the Jurassic zircons occupy an upper field in the diagram due to their higher Th values, which vary from about 300 ppm to more than 10,000 ppm. Meanwhile, the pre-Jurassic zircons of the same samples (open rhombs with similar colors) occupy a lower field, with Th values varying from 6 ppm to less than 1000 ppm. Moreover, the Th and U contents in the Jurassic zircons are related to the content of these two trace elements in their host rocks (Table 3). However, pre-Jurassic zircons coexisting in the same rocks do not present any relation with the composition of their host rocks, as can be seen by their lower Th/U values and the higher dispersion of their plots in Figure 7B. These differences in composition between Jurassic and pre-Jurassic zircons, compared with the composition of their host rocks, confirm the xenogenic character of these older zircon type with respect to their host magmatic rocks.

In Figure 7C, the U vs. Th compositions only of the Jurassic zircons from the Cóbdar and Algarrobo outcrops, in green and blue, respectively, are represented, together with the corresponding values of zircons from the Lugros and Almirez outcrops, in brown and red, respectively. The preserved magmatic areas of some zircons are represented as full dots, and those corresponding to recrystallized areas are represented as open squares. The aim of this figure is to compare the isotopic characteristics among the zircons from these four main Betic ophiolitic outcrops, which present a great similarity with each other. The higher number of recrystallized zircons in the Lugros and Almirez outcrops (squares vs. dots) than in those from Algarrobo and Cóbdar must be due to the higher degree and pervasiveness of metamorphism attained by the former, which affected both the texture and the local composition in the recrystallized areas, leading also to a decrease in their U and Th contents [3,7,64]. In Figure 7D, only the Pre-Jurassic zircons from Algarrobo, as full rhombs in blue, and from Cóbdar, as green full rhombs, are plotted, together with the unique zircon crystal from the Lugros outcrop dated as Precambrian [7,64]. The relative proportions between pre-Jurassic and Jurassic zircons in the Betic ophiolites are not related to the chemical compositions of their respective host magmas. In fact, sample P1-19, containing one unique Jurassic zircon among 23 pre-Jurassic crystals, presents an intermediate REE-normalized pattern between the plutonic and the volcanic rocks from the Algarrobo outcrop (Figure 5D), with an Yb_N value of higher than 10, indicating an origin from a spinel-mantle depth zone, similar to those of plutonic samples P1-13 and P1-62. Moreover, the CL aspect and post-magmatic alteration of the sole dated Jurassic zircon crystal in this sample is similar to those of sample P1-62 (Figure S2).

The U-Th plot of the zircons forming the current oceanic floor along the Mid-Atlantic Ridge (MAR) from about 13° N and 15° N [72], shown in Figure 7E, is similar to those deriving from other oceanic ridges characterized by slow-spreading development, such as that along the Atlantic Bank in the SWIR from 32°35′ S and 32°50′ S [73] and other dated oceanic floor zircons deriving from present-day slow- and ultra-slow-spreading mid-ocean ridges (MORs) [74]. The comparison between the U vs. Th zircon compositions from samples dredged along the MAR (Figure 7E) with the Jurassic zircons from the main Betic ophiolitic outcrops (Figure 7C) is indicative of a very plausible similar origin of the oceanic floor at the origin of these ophiolites and those generating the current slow-spreading ridges. Together with the current zircons dredged by Ref. [72] along the MAR, a big number of coexisting older zircons have been identified and dated, mainly Precambrian in age, and

are included in the host magmas that created the present oceanic floor. This is also the case in Ref. [75], which described some Paleozoic and Proterozoic zircons from the MAR drilled from exposed gabbros near the Kane fracture zone (at about 23°30′ N), and in Ref. [76], which also found unusually ancient zircons (100 to 330 and even 2230 Ma) together with other young ones (1.2–1.4 Ma) in the axial Mid-Atlantic Ridge zone (at about 5° N). These older zircons must have been incorporated into the current oceanic magmas, ascending from the asthenosphere to create the MAR, from some underlying layers traversed by these magmas in their ascending path at the oceanic surface. The interaction of the present oceanic magmas with the layers containing the older zircons took place without reaction between these older crystals and their host oceanic magmas, which would derive from a deeper source, leading to two different groups of zircons without overgrowth of the older one by the newly formed one (see the CL photos of these two zircon groups in Refs. [72,76]). Notably, we found a similar no-interaction relationship between the oceanic Jurassic magmas forming the Betic ophiolites and their pre-Jurassic, mainly Precambrian, hosted zircons (Figures S2–S4).

5.3. Oxygen Isotope Ratios in Magmatic Zircons of the Betic Ophiolites

Oxygen isotope analysis of zircons previously dated by U-Pb and representative of the Betic ophiolites are plotted in Figures 8 and 9, and shown in Table S15. In this table, the igneous Jurassic zircons are represented in black and the Precambrian ones in red. Moreover, in some samples in which it was possible to analyze $\delta^{18}O‰$ in some recrystallized areas, both under oceanic-floor conditions and in orogenic metamorphic conditions, these recrystallized values are differentiated with green and blue, respectively. Figures S4–S6 show representative cathodoluminiscence images of zircons selected for $\delta^{18}O$ determinations.

Figure 8 (upper panel) represents the $\delta^{18}O‰$ zircon values corresponding to the analyzed spots. Encircled numbers from 1 to 35 correspond to the selected areas of the CL-photos in Figures S4–S6. Figure 8 (lower panel) is a modification of the upper panel enlarging the horizontal axis to be able to represent the $\delta^{18}O‰$ values corresponding to the analyzed Precambrian zircons. The comparison of the CL aspect of the Jurassic and Precambrian zircons seems to indicate that the CL aspect of these two group of zircons is independent of their $\delta^{18}O$ zircon values. Moreover, in the Jurassic group the CL aspect of the zircons may be affected by changes in $\delta^{18}O‰$ values, and these are more marked when they were produced together with a change, more or less notable, in the U-Pb age between two analyzed areas of the same crystal. This fact is shown by spot 5 at the rim and spot 6 at the core of the same crystal from the P1-62 sample (Figure S4), which led to an inversion of ages between those corresponding to the core and rim of an igneous crystal, with an increase of $\delta^{18}O‰$ from 4.7 (rim) to 5.8 (core), but accompanied by a more marked decrease in radiometric age in the irregular whitish areas located at the core, which are plotted in field B of Figure 8. The preferential location in the zircons of this sample of the metasomatic alteration following the inner part along these crystals seems to have been favored by the presence of a twinned plan following their enlargement axis, which would facilitate oceanic fluid circulation. A similar change during the oceanic-floor metasomatism, not creating a rim surrounding the primitive igneous crystals but transforming them partly into more luminescent zircons, is well illustrated by spots 16.1 and 16.2 of the P1-11 sample from Algarrobo (Figure S2), represented in Figure 8 by spots 7 and 8, with about 6 Ma less than the corresponding igneous area.

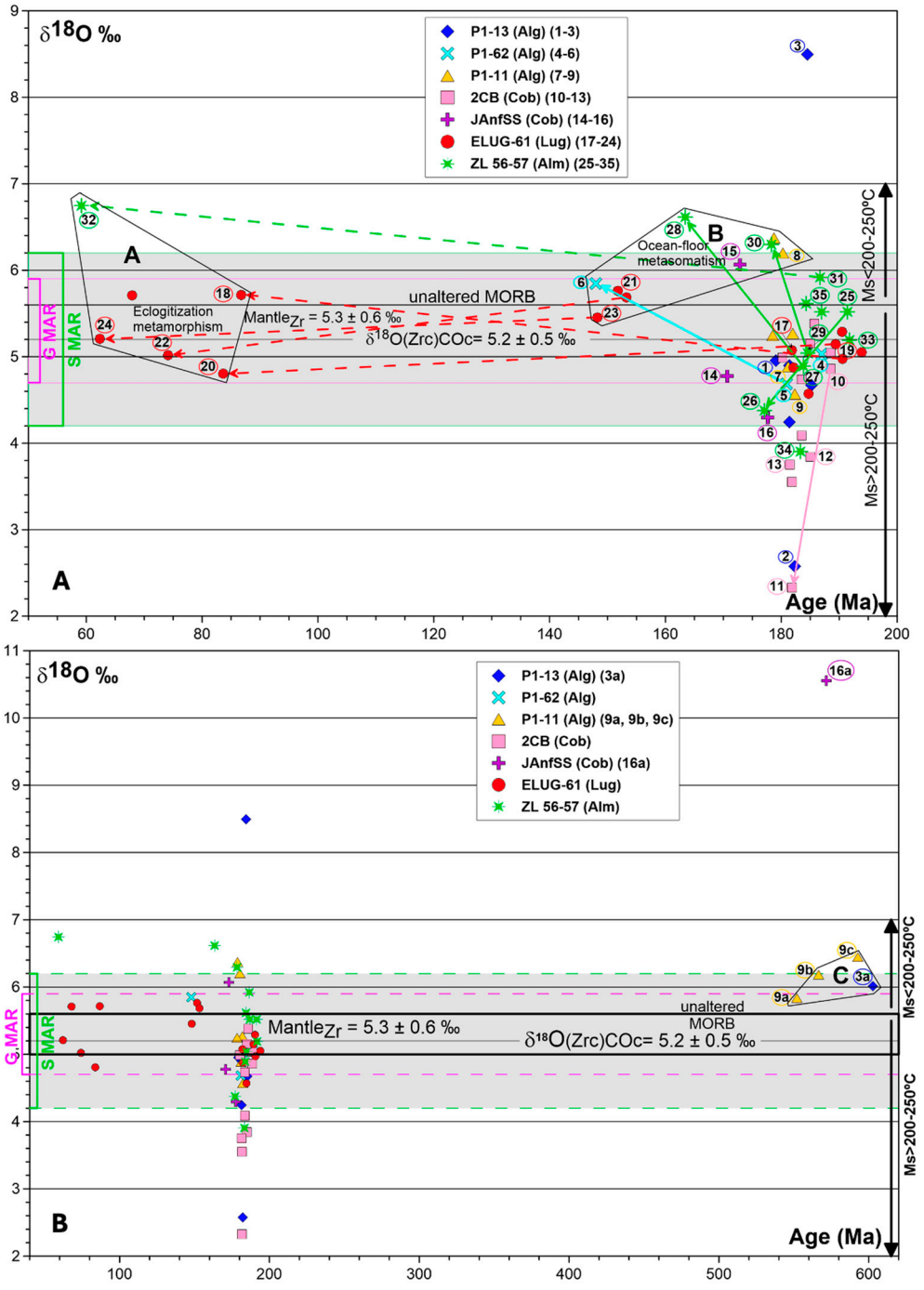


Figure 8. δ^{18}O‰ values versus age for zircon crystals of the Betic ophiolites from the Algarrobo, Cóbdar, Lugros, and Almirez outcrops. Field A (**A upper panel**) includes a group of Jurassic zircons locally transformed under high-pressure eclogite facies conditions. Field B (**A upper panel**) separates a group of igneous zircons affected by an ocean-floor metasomatic process. Field C (**B lower panel**) comprises four xenogenic zircon crystals of Precambrian age in metabasic rocks from Algarrobo and Cóbdar. The horizontal range in grey, comprising δ^{18}O zircons of between 4.7 and 5.9‰, indicates the range for zircon in gabbros dredged from the MAR ridge (G MAR) under high-temperature equilibrium with primitive igneous rocks and mantle [77,78]. δ^{18}O‰ zircon = 5.2 ± 0.5 is the average value of 197 Zrs from 43 rocks from MAR 15° N and 30° N, and SWIR at 57° E [79]. G-MAR and S-MAR are the ranges of δ^{18}O‰ zircon of gabbros and dolerite dikes in serpentinites, respectively, dredged along these slow-spreading mid-ocean ridges. Ms values > 200–250 °C and Ms < 200–250 °C indicate the T[a] range of metasomatism on the oceanic igneous zircons in subsolid conditions according to Ref. [79].

In other crystals, such as in those from the Lugros outcrop (Figure S5), the effect of the oceanic metasomatism did not consist of the development of a zircon rim, but rather of the loss of the oscillatory igneous zoning, characteristic of the preserved igneous areas, together with a corresponding decrease in the U-Pb age of the metasomatized areas. Analogously, in the Almirez rodingites (Figure S6), the metasomatized areas under oceanic conditions formed irregular unzoned rims surrounding the igneous zoned cores. In these rodingites, the igneous core (25) was overgrown by its rim (26) in a metasomatism under high-T conditions, as shown in Figure 8 by the descending arrow joining these two spots. Meanwhile, the cores (spots 27 and 29) were overgrown by a metasomatism of lower T, as shown by the plot of their respective rims (28 and 30), joined with their cores by two ascending arrows.

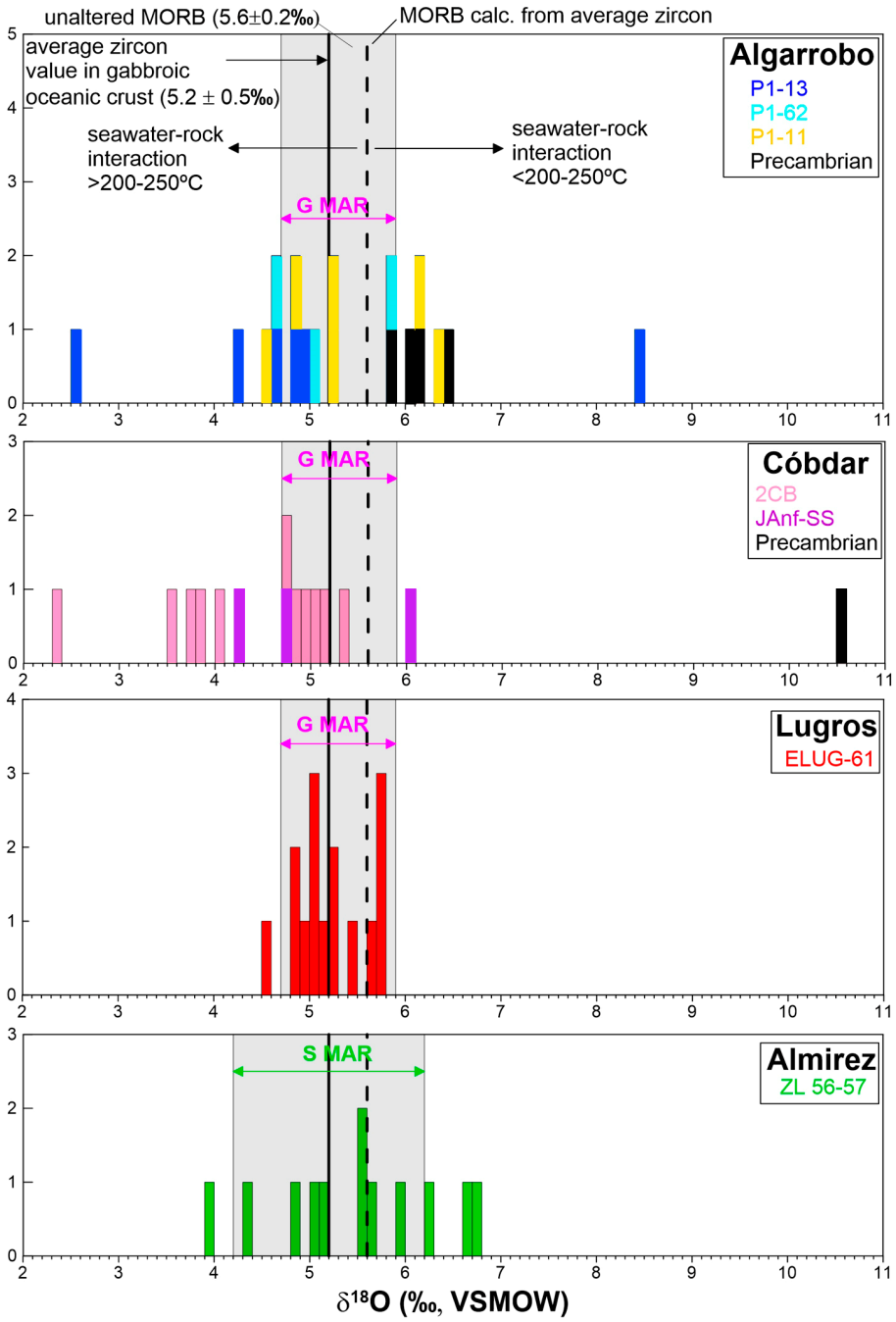


Figure 9. Histograms comparing $\delta^{18}O$‰ values of the zircons analyzed from the different Betic ophiolites outcrops: Algarrobo, Cóbdar, Lugros, and Almirez. Compositional fields as in Figure 8.

The $\delta^{18}O$ isotopic ratios in the Jurassic zircons of the Betic ophiolites compared with those presented by similar igneous rock types dredged from the Central Atlantic oceanic floor, mainly at 15° N and 30° N [79], at the MARK area near the Kane fracture transform [78], and in the SWIR at 57° E [73], show a great similarity with the gabbros and dikes in serpentinites dredged in these ultra-slow spreading ridges, as shown in Figure 8. As can be seen in this figure, for some zircon crystals, the increase in $\delta^{18}O$ values due to low-T metasomatism was accompanied by a decrease in age, suggesting the existence of a late ocean-floor metasomatic process, leading to a very pervasive effect that was accompanied by a variable decrease in age up to about 150 Ma in some of these outcrops. This process is well illustrated, for example, by spots 5 and 6 of sample P1-62, comparing in Figures 8 and S4 their marked CL aspect variation, increase in $\delta^{18}O$ (from 4.7 to 5.8), decrease in age (from 181 to 148 Ma), and decrease in U content (Table S12). A similar comparison between two areas from the same zircon crystal can be made between spots 27 and 28 (Figure S6) for igneous and oceanic-floor conditions, respectively, of the metarodingite from the Almirez outcrop (ZL56-57), which underwent an increase in $\delta^{18}O$ (from 4.9 in spot 8.1 to 6.6 in spot 8.2) and a decrease in age of about 20 Ma (field B in Figure 8), accompanied by a decrease in U content. The zircons of this group, with the decrease in their U-Pb ages, are represented in area B of Figure 8 and interpreted as being due to the ocean-floor metamorphism and metasomatism, which were previously identified in some outcrops of the Betic ophiolites [7,64].

In area A of Figure 8, zircon crystals from the Lugros and Almirez outcrops are grouped, which are interpreted as having recrystallized during the orogenic alpine metamorphism, which was more pervasive in these two outcrops but which also affected, at least at the thin-section scale, to samples from the Cóbdar and Algarrobo outcrops [3,7,64]. Some zircon crystals of group A, such as the one in spot 18, with a $\delta^{18}O$ of 5.7 and 87 Ma, represent a small recrystallization area with higher luminescence, in igneous zircon spot 17, with a $\delta^{18}O$ of 5.1 and an age of 182 Ma. When orogenic alpine metamorphism areas in zircon crystals are compared with other areas corresponding to the previous ocean-floor metasomatism, the $\delta^{18}O$ values decrease, as can be seen between spot 21, with an age of 153 Ma and a $\delta^{18}O$ of 5.7, and spot 22, with an age of 74 Ma and a $\delta^{18}O$ of 5.0.

In Figure 8, the $\delta^{18}O$ values of five Precambrian zircons in some metabasite samples from the Algarrobo and Cóbdar outcrops are plotted. Zircon crystals enumerated as 9a, 9b, and 9c in this figure (lower panel) come from metabasalt P1-11 from the Algarrobo outcrop, and their $\delta^{18}O$ values, varying from 5.8 to 6.4, are near some of the Jurassic zircons $\delta^{18}O$ values that underwent oceanic-floor metasomatism, although their size and convoluted CL aspect are different to those of the Jurassic zircons in the same sample (see CL photos 7 to 9c in Figure S4). The $\delta^{18}O$ values of these Precambrian zircons seem to indicate that they underwent oceanic-floor metasomatism at low T (<250–200 °C), similar to the oceanic-floor metasomatic conditions that also affected the Jurassic zircons.

In the histogram of Figure 9, the $\delta^{18}O$ values of the analyzed zircon spots are represented. Most of the zircons from gabbroic and basaltic metabasites of the Betic ophiolitic outcrops (Algarrobo, Cóbdar, and Lugros) are plotted in the range of 4.7 to 5.9 $\delta^{18}O$, matching the MAR gabbros (G MAR) studied by Refs. [78,79]. The basic intrusive dikes in serpentinites from the Almirez outcrop (rodingites) present a higher dispersion of $\delta^{18}O$ values, mainly in the 4.2 to 6.2 range, similar to the types of dykes in the MAR serpentinites [78,79].

5.4. Trace Elements Geochemistry of Zircons of the Betic Ophiolites

REE analyses were conducted on some of the dated zircon areas of the analyzed samples from the Cóbdar, Algarrobo, Lugros, and Almirez outcrops. These new REE analyses were complemented with the published results corresponding to the Lugros

zircons [64]. The data are plotted in Figure 10, separating the seven analyses from areas in which the igneous characteristics are better preserved (Figure 10A, Table S16) from the other seven analyses from areas that are more clearly recrystallized (Figure 10B, Table S16).

In the inset of Figure 10, the symbols and colors corresponding to the REE-normalized pattern of each one of the analyzed samples is represented, followed by the different analyzed spots and a number in parenthesis, corresponding to the number of its corresponding CL photo in Figures S4–S6.

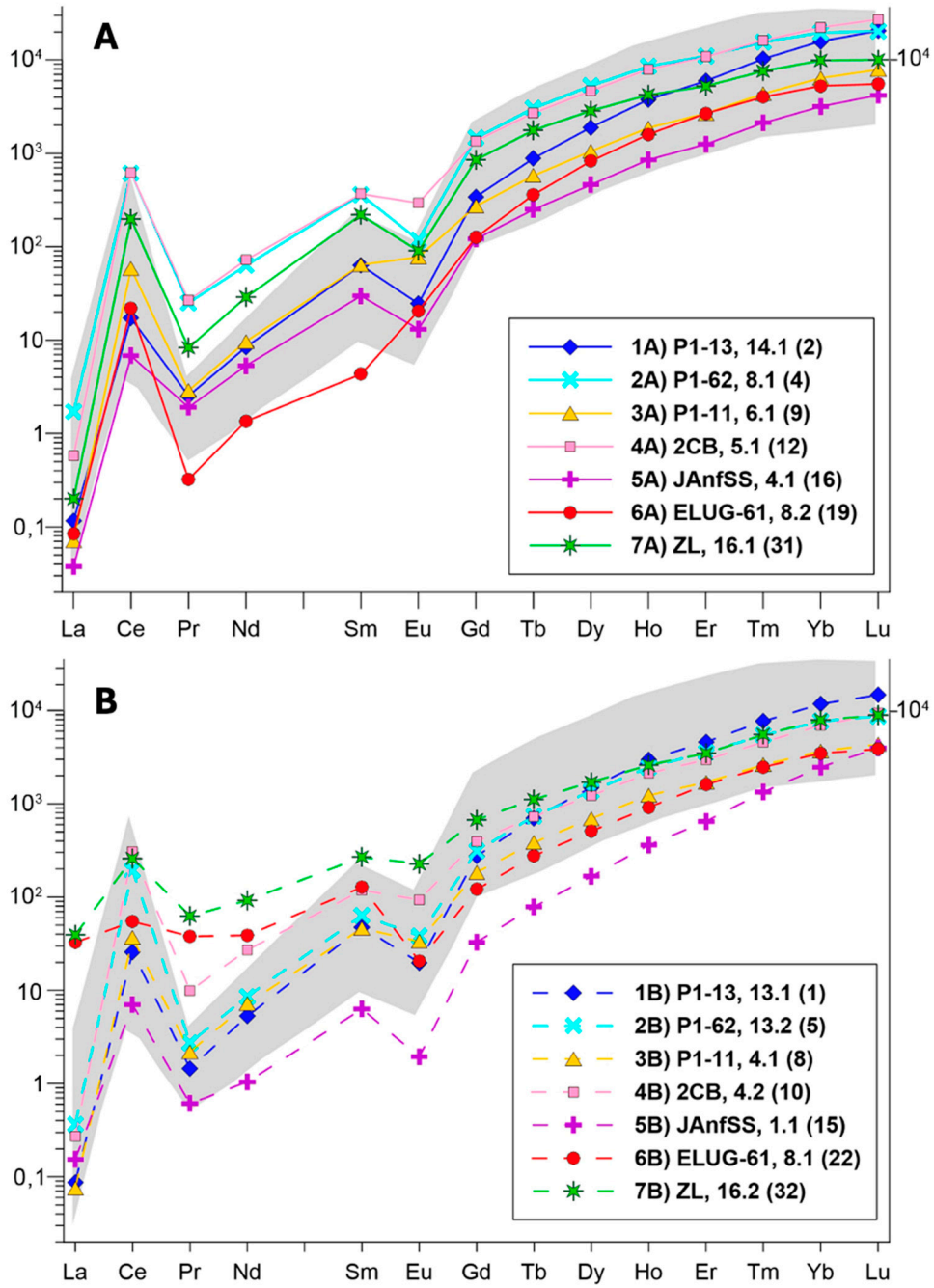


Figure 10. REE-normalized patterns of spots in zircon crystals in igneous (**A**) and recrystallized (**B**) areas. The grey field represents the REE compositions of MORB gabbros from oceanic crust according to Ref. [74].

The recrystallization process, visible in the CL images, did not significantly disturb the igneous REE patterns, except for the LREE enrichment in some areas surrounding vesicles and in some areas affected by a more marked orogenic metamorphism, such as

those corresponding to numbers 10, 22, and 32 in Figure 10B and in the CL photos of Figures S4–S6. Nevertheless, in each crystal, the REE content from Lu to Eu is normally lower in the recrystallized zones than in the zones corresponding to well-preserved igneous areas commonly characterized by oscillatory-zoned rims, as in CL photos 19 and 31 of the same zircons. The extent of this decrease in REE concentrations is normally more notable in the areas recrystallized by orogenic metamorphism than in those affected by oceanic-floor metasomatism. However, in both cases a decrease in REE values in the interval from Eu to Ce and a slight increase in LREE value were observed, as shown in Figure 10B compared with Figure 10A. These variations in the REE contents of limited areas in some zircons, in comparison to their igneous zones, may be interpreted as being due to REE re-equilibration of the igneous zircons by processes of metamorphic recrystallization, favored by fluids filling the vesicles in these crystals or surrounding them during oceanic floor metasomatism.

In addition to the minor changes in the REE patterns previously described, other trace elements, such as Y and Hf, present in the recrystallized areas evidence some Y depletion and Hf enrichment, which is similar to the changes reported by Refs. [80,81] in recrystallized areas of igneous zircon in granulite facies conditions.

6. Development and Evolution of the Betic Tethys

The Alpine–Apennine ages in Figure 11 are based on the compilation of U-Pb radiometric dating, together with radiolarian ages identified in the sedimentary sequence of some poorly metamorphosed ophiolitic outcrops, published by Refs. [82,83].

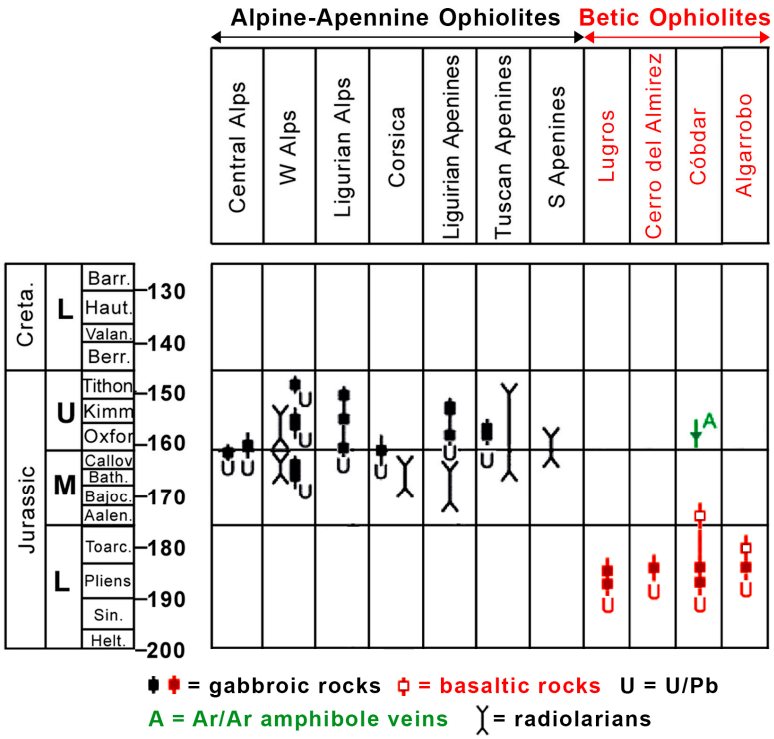


Figure 11. U-Pb igneous ages in oceanic mafic rocks from the Alpine–Apennine ophiolites (black), compiled by Refs. [82–84], and those from the Betic ophiolites (red) in this paper and in Ref. [3].

We added to the Alpine–Apennine ages in Figure 11 the U-Pb dating of Ref. [84] for ophiolitic gabbros from the Ligurian Apennines, with have similar ages of 160–165 Ma.

In the case of the Betic ophiolites, we have represented in red the margins of absolute ages obtained in this study, complemented with previous data [3,7]. The Betic U-Pb radiometric ages of zircons from gabbroic rocks are about 20 Ma older than the zircons in

similar rock types from the Alps, Corsica, and Apennine ophiolites, as we noted before for the Lugros and Almirez outcrops in Ref. [7]. Also in this figure, green represents the Middle Jurassic age (158 ± 4.5 Ma), obtained with an Ar/Ar laser probe in millimetric veins filled with high-gradient brown amphibole of oceanic-floor metamorphism [3], identified mainly as Ti-pargasite and kaersutite containing numerous halite inclusions [45,85] in basalts from Cóbdar, dated by U-Pb zircons as Lower–Middle Jurassic.

In Figure 12A, we indicate the probable location of the Betic Tethys (BT) on the initial oceanic-floor branch (dark blue color) developed from the Pliensbachian to the Aalenian, according to our radiometric U-Pb dating (Figure 11), which would be coetaneous with the Central Atlantic opening from about 12° N to 22° N. The red strips represented by Ref. [86] during this stage would correspond, in agreement with the U-Pb zircon ages of the Alpine–Apennine ophiolites (Figure 11), to different rifting zones, which, during the Tithonian stage, would give place to different sectors of the Ligurian and Alpine Tethys, coetaneous to the Central Atlantic oceanic floor, from 20° N to 35° N (Figure 12B).

The Alpine–Apennine oceanic floors must have been developed from the Bathonian up to the Tithonian age, according to the U-Pb dating of zircons from their ophiolites. Meanwhile, in the Betic ophiolites, we have not found zircons with U-Pb ages corresponding to this period, with the most recent radiometric age obtained being that from the brown amphibole veins, dated as Oxfordian (158 ± 4.5 Ma). These amphibole veins were created by ocean-floor metamorphism in Lower to Middle Jurassic basalts from Cóbdar, where the most recent volcanic level dated, interlayered with the sedimentary cover, yielded an age of 174 Ma. Nevertheless, similar brown amphibole relics have also been identified in metabasalts from the Lugros and Algarrobo outcrops [3,45]. These data suggest that the Betic oceanic floor, whose accretion period began in the Pliensbachian, probably would continue its expansion, undergoing high-gradient ocean-floor metamorphism [3] during the accretion period of the Ligurian and Alpine Tethys (Figure 12B). Whatever the case, we have not identified any ophiolite outcrop located to the west of the Betic ophiolites, which could derive from a Middle–Upper Jurassic oceanic section, as suggested by Ref. [86], although the meta-sedimentary cover overlying these ophiolites could have yielded these more recent ages [30].

A red transversal line from V (NFC Lower Unit—Veleta) to M (NFC Upper Unit—Mulhacén) is drawn in Figure 12 to indicate the more probable setting of the Betic ocean accretion from the Pliensbachian (dark blue strip at the rims) to the Middle–Upper Jurassic (lighter blue in the inner band) between their continental margins.

Figure 13 shows, with different green bands, the progressively accreted levels from the external to the inner part of the Betic ocean, corresponding to the five magmatic levels identified by U-Pb zircons dating of their metabasic host rocks from the Algarrobo (Figure 13, upper panel) and Cóbdar (Figure 13, lower panel) outcrops. In agreement with the U-Pb ages obtained, the minimum accretion period could be around 7.3 Ma for the Algarrobo outcrop (184.3 Ma for the older sample to probably 177 Ma for the youngest one) and around 13.1 Ma (from 186.9 to 173.8 Ma) for the Cóbdar outcrop. Considering around 12 mm/yr as the most probable spreading rate during the development of the Betic oceanic floor, corresponding to an ultra-slow ridge, and according to the rotation model of Ref. [86], the approximately attained extension of the two oceanic sections shown in Figure 13 could be around 87.6 km for the Algarrobo section and 157.2 km for the Cóbdar section.

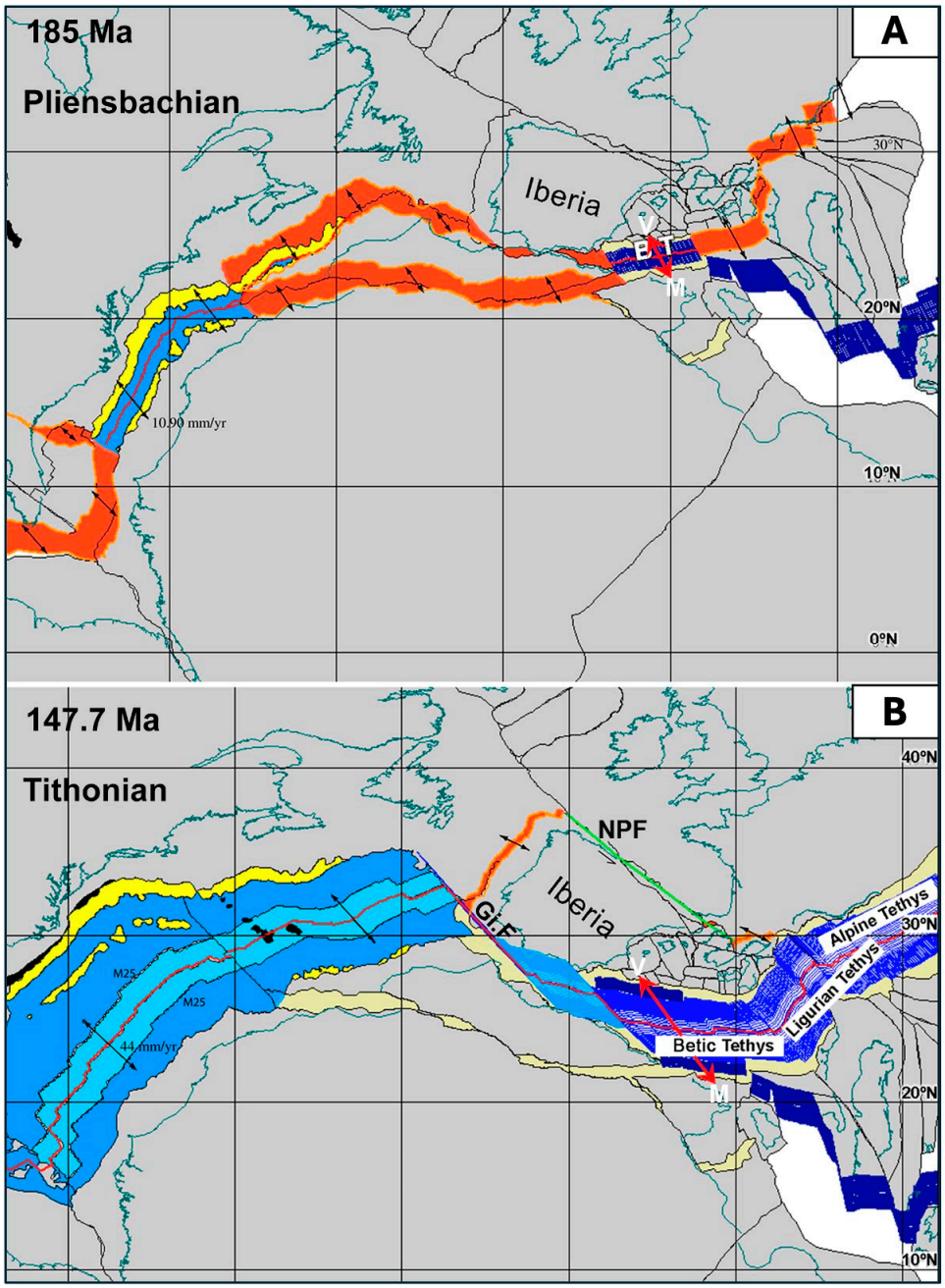


Figure 12. Eastern section of the Paleogeographic reconstruction of the Western Tethys and Central Atlantic from Ref. [86] at (**A**) 185 Ma (Pliensbachian) and (**B**) 147.7 Ma (chron 21, Tithonian). Gi.F = Gibraltar Fault; NPF = North Pyrenean Fault.

Figure 14A presents a block diagram illustrating the hypothetical paleogeography of the Betic ocean during its Lower to Middle Jurassic accretion period. This basin formed by distension between the Iberian and African crustal blocks, which triggered the ascent and partial melting of the asthenospheric mantle. Betic ocean development initiated in the Pliensbachian, as supported by our U-Pb zircon dating of the Betic ophiolites and the paleogeographic reconstruction of the Western Tethys and Central Atlantic from Ref. [86], as shown in Figure 14A. This accretion period spans at least from 187 to 174 Ma (Figure 13). The Betic oceanic floor would separate the Veleta and Mulhacén crustal margins. In Figure 14A, different rectangles extended from gabbros (green) to basalts (red) represent a suggested relative location in the Betic ocean of the dated samples from the Lugros (Lu), Cóbdar (Cb), and Algarrobo (Ag) outcrops. The older dated gabbros in the Lugros and

Cóbdar outcrops are 187 Ma, while in the Algarrobo outcrop, located at the eastern end of the Lower Jurassic Betic ocean, the age of the older dated gabbros is 184 Ma. These older ages probably represent the time corresponding to the Pliensbachian stage of the Gondwana breakup between the Iberian and African continental blocks, which would also have led to the beginning of the Betic ocean development and its evolution from a rifting to a drifting transition. The differences in the lower gabbro level identified between the Cóbdar (187 Ma) and Algarrobo outcrops (184 Ma) could represent a progression in the opening of the Betic ocean toward the northeast, from the Pliensbachian to the Tithonian age, similar to that proposed by Ref. [87] for the opening of the North Atlantic Ocean between the Iberia and Newfoundland rifts from southwest to northeast along the Lower Cretaceous at about 125 Ma.

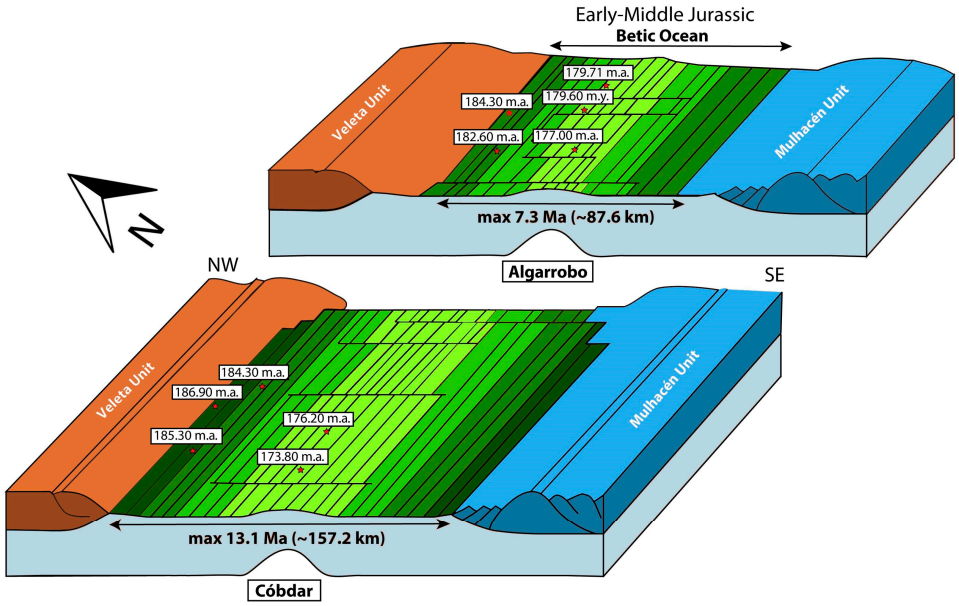


Figure 13. Interpretative reconstruction of the accretion bands forming the Betic ocean. (**Upper panel**): Algarrobo; (**lower panel**): Cóbdar.

As depicted in Figure 14A by a bigger rectangle, the Almirez outcrop (Az) led to exhumation to the oceanic floor of serpentinized peridotites, probably delimited by a detachment fault, created by an oceanic core complex (Almirez OCC) similar to the Atlantis Massif, at the intersection of the Mid-Atlantic Ridge (MAR) and the Atlantis Transform Fault [88,89]. These oceanic core complexes have also been described in the Tethyan ophiolites [90–92]. In the Almirez OCC, ultramafic rocks were traversed during the opening of the Betic ocean by dolerite dikes, with a similar composition as the basic rocks forming the surrounding cogenetic gabbros and basalts, although affected by a rodingitization process [3,7,64,68,93,94], which mainly originated during the oceanic serpentinization process. The changes in chemical and mineralogical compositions in both basic dykes and their host ultramafic rocks during the rodingitization process also progressed in the orogenic metamorphism, although less intensely, up to the creation of the meta-rodingites. These transformations also affected their zircon crystals, which were dated to 184 Ma, and their rodingitization process presented a climax at 177 Ma (Figrues 7, 8 and S6). Moreover, the later orogenic partial transformations have also been registered in the coetaneous gabbroic rocks, beginning at the Cenozoic eclogitization stage (Figure 14B).

Finally, Figure 15 shows the dismembering of the AlKaPeCa (Alboran, Kabilies, Peloritani, Calabria) microplate (Figure 15A) and the translation of the Alboran block (AB) toward the SW (Figure 15B) until reaching its present location [5], forming the Internal Zones of the Betic and Rif Cordilleras, followed by the stage of collision between the Iberian and

African crustal blocks (Figure 15C). This model of tectonic evolution along the Cenozoic, consisting of subduction rollback of the oceanic floor from the Oligocene to present, led to a similar drifting to the Betic–Rif Cordillera and to the Corsica, Kabylies, Peloritani, and Calabria blocks, which were finally accreted to the adjacent continents [3].

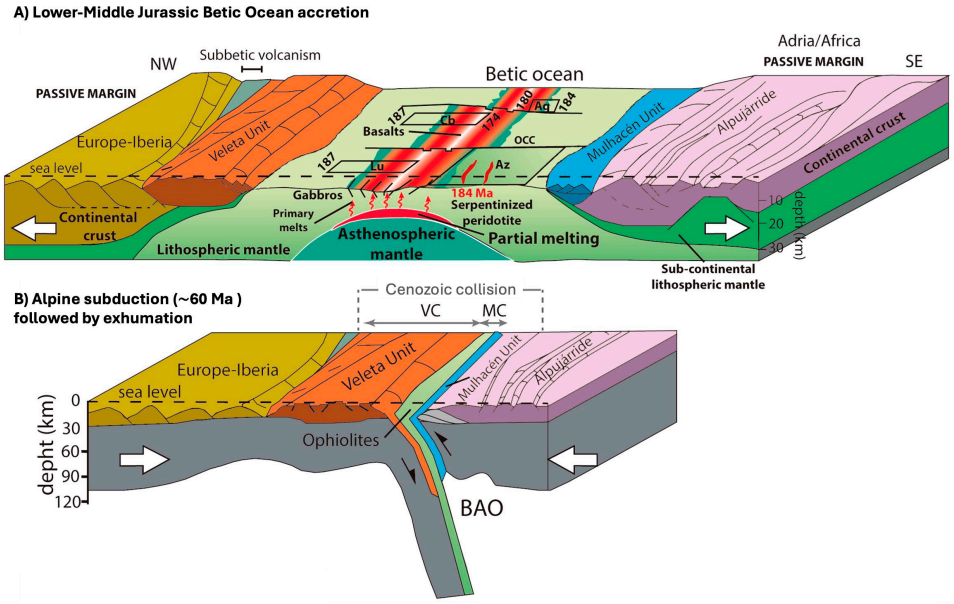


Figure 14. Tectono-metamorphic Mesozoic to Cenozoic evolution of Betic Units. Stage (**A**) shows the inferred paleogeography of the Betic ocean from the Lower to Middle Jurassic accretion period, followed in stage (**B**) by an Eocene compressive tectonic setting that led to the subduction and eclogitization of the Betic ophiolites.

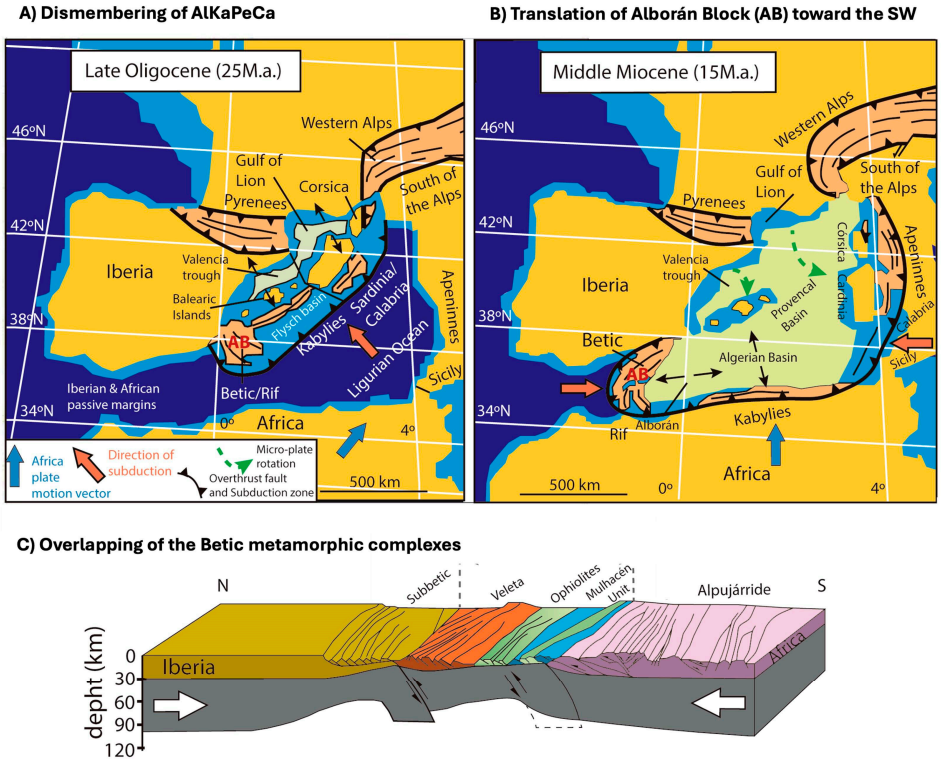


Figure 15. Tectono-metamorphic Cenozoic to present-day evolution of Betic Units. Stages (**A**,**B**) show the dismembering of the AlKaPeCa microplate and the translation of the Alboran block (AB) toward the SW, followed by stage (**C**), representing the collision between the Iberian and African crustal blocks.

Therefore, our integrated dataset fundamentally revises the existing tectonic models by demonstrating that the Nevado-Filábride Complex comprises a fragment of a single, long-lived Jurassic ocean basin, thereby providing a cohesive framework that reconciles the Mesozoic geodynamic evolution of the westernmost Alpine Tethys with the broader Atlantic rift system.

7. Conclusions

- Petrological and geochemical analyses of the metabasic rocks within the Betic ophiolites reveal the MORB affinity of their various igneous lithotypes. These include olivine–pyroxene gabbros, dolerites, and basalts, as identified in all four studied outcrops: Lugros, Almirez, Cóbdar, and Algarrobo.
- Their zircons, dated by U-Pb with SHRIMP and ranging in age from the Lower to the Middle Jurassic, have also allowed us to distinguish several magmatic levels in the Cóbdar and Algarrobo outcrops, as well as a formation period for the Betic oceanic floor ranging from approximately 187 to 173 Ma. This formation period was followed by the development of the overlying sedimentary sequence.
- Alongside the Jurassic zircons, pre-Jurassic xenocrystic zircon crystals, mainly of Precambrian age, were identified, primarily in samples from the Algarrobo outcrop. These xenocrysts are similar in age and chemical composition to those coexisting with modern volcanism dredged from the Mid-Atlantic Ridge (MAR) near fracture zones and from other ultra-slow ridges like the Southwest Indian Ridge (SWIR) at the Atlantic Bank. The similarity in age and chemical composition of the Precambrian xenocrystic zircon of the Betic ophiolites and those dredged from the MAR and SWIR suggests a similar tectonic setting for magmatism in both the Jurassic Betic Ocean and contemporary ultra-slow oceanic ridges.
- The $\delta^{18}O$ isotopic ratios of zircons from the Betic ophiolites, sampled from gabbros, basalts, and dolerite dykes intruding into serpentinites, show strong similarity to values from zircons in analogous igneous rocks dredged from ultra-slow oceanic ridges, such as the MAR and SWIR.
- Additionally, some zircon crystals from the Betic ophiolites preserve local variations in their $\delta^{18}O$ values. These variations record two distinct metamorphic events: an earlier one dated to ~150 Ma, interpreted as oceanic floor metamorphism, and later Cenozoic ages, attributed to the orogenic metamorphism that affected the host rocks.
- The chondrite-normalized REE patterns of Jurassic igneous zircons from the Betic ophiolites are consistent with those of zircons from oceanic crust. Furthermore, their more recrystallized domains, commonly found surrounding vesicles, exhibit a slight depletion in HREE and Y, alongside a local increase in LREE and Hf values. This geochemical signature is also similar to that observed in other Tethyan ophiolites.
- The interpretative location of the four studied Betic ophiolitic outcrops (Lugros, Cóbdar, Algarrobo, and Almirez) within a hypothetical reconstruction of the Jurassic Betic Ocean is based primarily on their U-Pb ages. These ages range from 187 to 180 Ma for gabbros and basalts in the first three outcrops. The dolerite dikes that intruded into the Almirez ultramafic rocks under oceanic conditions yielded an age of 184 Ma. Therefore, these ultramafic rocks were already exhumed at that time into the ocean floor, forming an oceanic core complex.

Supplementary Materials: The following supporting information can be downloaded at: https://www.mdpi.com/article/10.3390/geosciences15100406/s1, and includes Analytical Methods, Figures S1 to S6, and Tables S1 to S16, with geochemical and geochronological datasets of the rocks mentioned in the text.

Author Contributions: Conceptualization: E.P., A.D.d.F., M.A.D.P., and J.M.N.; methodology: E.P., A.D.d.F., M.A.D.P., and J.M.N.; validation: E.P., A.D.d.F., M.A.D.P., and J.M.N.; writing—original draft preparation: E.P. and J.M.N.; review and editing: E.P. and J.M.N. All authors have read and agreed to the published version of the manuscript.

Funding: This research was funded by the University of Huelva (Environmental Mineralogy and Geochemistry Group).

Data Availability Statement: The original contributions presented in this study are included in the article/Supplementary Material. Further inquiries can be directed to the corresponding author.

Acknowledgments: J.M.N. would like to express his gratitude to his colleagues from the Department of Earth Sciences at the University of Huelva for their stimulating discussions on the geology of the Nevado-Filábride Complex during the long field campaigns over the past four years of geological mapping camps in Sierra de los Filabres with our Geology students, which have been both enriching and inspiring.

Conflicts of Interest: The authors declare no conflicts of interest.

References

1. Bouillin, J.P.; Durand-Delgá, M.; Olivier, P.H. Betic-Rifain and Tyrrenian Arcs: Distinctive features, genesis and development stages. In *The Origin of Arcs*; Wezel, F.C., Ed.; Elsevier: Amsterdam, The Netherlands, 1986; pp. 281–304.
2. Guerrera, F.; Martin-Algarra, A.; Perrone, V. Late Oligocene–Miocene syn-/-late orogenic successions in Western and Central Mediterranean Chains from the Betic Cordillera to the Southern Apennines. *Terra Nova* **1993**, *5*, 525–544. [CrossRef]
3. Puga, E.; de Federico, A.D.; Fanning, M.; Nieto, J.M.; Martínez-Conde, J.Á.R.; Puga, M.Á.D.; Lozano, J.A.; Bianchini, G.; Natali, C.; Beccaluva, L. The Betic Ophiolites and the Mesozoic Evolution of the Western Tethys. *Geosciences* **2017**, *7*, 31. [CrossRef]
4. Lonergan, L.; White, N. Origin of the Betic –Rif mountain belt. *Tectonics* **1997**, *16*, 504–522. [CrossRef]
5. Rosenbaum, G.; Lister, G.S.; Duboz, C. Reconstruction of the tectonic evolution of the western Mediterranean since the Oligocene. *J. Virtual Explor.* **2002**, *8*, 107–130. [CrossRef]
6. Puga, E.; Nieto, J.M.; De Federico, A.D.; Nieto, J.M. Tectono-stratigraphic subdivison and petrological characterisation of the deepest complexes of the Betic Zone: A Review. *Geodin. Acta* **2002**, *15*, 23–43. [CrossRef]
7. Puga, E.; Fanning, M.; de Federico, A.D.; Nieto, J.M.; Beccaluva, L.; Bianchini, G.; Puga, M.A. Petrology, geochemistry and U-Pb geochronology of the Betic Ophiolites: Inferences for Pangaea break-up and birth of the westernmost Tethys Ocean. *Lithos* **2011**, *124*, 255–272. [CrossRef]
8. Vergés, J.; Fernández, M. Tethys–Atlantic interaction along the Iberia–Africa plate boundary: The Betic–Rif orogenic system. *Tectonophysics* **2012**, *579*, 144–172. [CrossRef]
9. Michard, A.; Mokhtari, A.; Chalouan, A. New ophiolite slivers in the External Rif belt, and tentative restoration of a dual Tethyan suture in the western Maghrebides. *Bull. Société Géologique Fr.* **2014**, *185*, 313–328. [CrossRef]
10. Platt, J.P.; Anczkiewicz, R.; Soto, J.I.; Kelley, S.P.; Thirlwall, M. Early Miocene continental subduction and rapid exhumation in the western Mediterranean. *Geology* **2006**, *34*, 981–984. [CrossRef]
11. Vera, J.A.; Martín-Algarra, A. Cadenas Béticas: Divisiones mayores y nomenclatura. In *Geología de España*; Vera, J.A., Ed.; SGE-IGME: Madrid, Spain, 2004; pp. 348–350.
12. Porkoláb, K.; Matenco, L.; Hupkes, J.; Willingshofer, E.; Wijbrans, J.; Lantman, H.; van Hinsbergen, D. Tectonic Evolution of the Nevado-Filábride Complex (Sierra de Los Filábres, Southeastern Spain): Insights from new structural and geochronological data. *Tectonics* **2022**, *41*, e2021TC006922. [CrossRef]
13. Linthout, K.; Vissers, R.L.M. On the classification of tectonic units in the Nevado-Filabrjde Complex of the northern Sierra de los Filabres, Betic Cordilleras, SE Spain. *Geol. Mijnb.* **1979**, *58*, 49–56.
14. Poulaki, E.M.; Stockli, D.F. The paleotectonic evolution of the western Mediterranean: Provenance insights from the internal Betics, southern Spain. *Front. Earth Sci.* **2022**, *10*, 929502. [CrossRef]
15. Martínez-Martínez, J.M. Evolución tectono-metamórfica del Complejo Nevado-Filábride en el sector de unión entre Sierra Nevada y Sierra de los Filabres (Cordilleras Béticas, España). *Cuad. Geol. Univ. Granada* **1986**, *13*, 194.
16. Martínez-Martínez, J.M.; Soto, J.I.; Balanyá, J.C. Orthogonal folding of extensional detachments: Structure and origin of the Sierra Nevada elongated dome (Betics, SE Spain). *Tectonics* **2002**, *21*, 1–22. [CrossRef]
17. Zeijlmans van Emmichoven, C.P.A. Geologische Onderzoekingen in the Sierra de los Filabres (Provincie Almeria, Spanje). Ph.D. Thesis, University Delft, Delft, The Netherlands, 1925; p. 160.
18. Brouwer, H.A. Zur Geologie der Sierra Nevada. *Int. J. Earth Sci.* **1926**, *17*, 118–137. [CrossRef]

19. Fallot, P.; Faure-Muret, A.; Fontboté, J.M.; Solé Sabaris, L. *Estudios Sobre las Series de Sierra Nevada y de la Llamada Minschungszone*; Publicaciones del Laboratorio de Geología de la Universidad de Granada: Granada, España, 1961; p. 537.
20. Laborda-López, C.; Aguirre, J.; Donovan, S.K. Surviving metamorphism: Taphonomy of fossil assemblages in marble and calc-silicate schist. *Palaios* **2015**, *30*, 668–679. [CrossRef]
21. Rodríguez-Cañero, R.; Jabaloy-Sánchez, A.; Navas-Parejo, P.; Martín-Algarra, A. Linking Palaeozoic palaeogeography of the Betic Cordillera to the Variscan Iberian Massif: New insight through the first conodonts of the Nevado-Filábride Complex. *Int. J. Earth Sci.* **2017**, *107*, 1791–1806. [CrossRef]
22. Nijhuis, H.J. Plurifacial Alpine Metamorphism in the Southeastern Sierra de los Filabres South of Lubrín, SE Spain. Ph.D. Thesis, University Amsterdam, Amsterdam, The Netherlands, 1964; p. 151.
23. Voet, H.W. Geological Investigations in the Northern Sierra de los Filabres, Around Macael and Cóbdar, SE Spain. Ph.D. Thesis, University Amsterdam, Amsterdam, The Netherlands, 1967; p. 122.
24. Poulaki, E.M.; Stockli, D.F.; Shuck, B.D. Pre-Subduction Architecture Controls Coherent Underplating During Subduction and Exhumation (Nevado-Filábride Complex, Southern Spain). *Geochem. Geophys. Geosystems* **2023**, *24*, e2022GC010802. [CrossRef]
25. Puga, E. The Betic Ophiolitic Association (Southeastern Spain). *Ofioliti* **1990**, *15*, 97–117.
26. Brouwer, H.A. Über die Struktur der penninischen Zone in den betischen Kordilleren. *Geol. Rundsch.* **1934**, *25*, 383–387. [CrossRef]
27. Barbero, E.; Dilek, Y.; Festa, A.; Saccani, E. Ophiolites and ophiolitic mélanges: Archives of Precambrian and Phanerozoic plate tectonics in orogenic belts. *Geosystems Geoenvironment* **2023**, *2*, 100191. [CrossRef]
28. Laborda-López, C.; Marchesi, C.; Sánchez-Vizcaíno, V.L.; Gómez-Pugnaire, M.T.; Dale, C.W.; Jabaloy-Sánchez, A.; Padrón-Navarta, J.A.; Román-Alpiste, M.J.; Garrido, C.J. Geochemical evolution of rodingites during subduction: Insights from Cerro del Almirez (southern Spain). *Lithos* **2020**, *370*, 105639. [CrossRef]
29. López Sánchez-Vizcaíno, V.; Franz, G.; Gómez-Pugnaire, M.T. The behaviour of Cr during metamorphism of carbonate rocks from the Nevado-Filabride Complex, Betic Cordilleras, Spain. *Can. Mineral.* **1995**, *33*, 85–104.
30. Tendero, J.; Martín-Algarra, A.; Puga, E.; Díaz de Federico, A. Lithostratigraphie des métasédiments de l'association ophiolitique Nevado-Filábride (SE Espagne) et mise en évidence d'objets ankéritiques évoquant des foraminifères planctoniques du Crétacé: Conséquences paléogéographiques. *Comptes Rendus L'académie Sci. Série 2 Mécanique Phys. Chim. Sci. L'univers Sci. Terre* **1993**, *316*, 1115–1122.
31. López Sánchez-Vizcaíno, V.; Gomez-Pugnaire, M.T. Metamorphism of the Nevado-Filábride Complex. In *The Geology of Iberia: A Geodynamic Approach*; Quesada, C., Oliveira, J.T., Eds.; The Alpine Cycle: East Sussex, UK, 2019; Volume 3, pp. 530–544.
32. Nieto, J.M. Petrología y Geoquímica de los Ortogneises del Complejo del Mulhacén, Cordilleras Béticas. Ph.D. Thesis, University Granada, Granada, Spain, 1996; p. 211.
33. Bicker, R.E. Geological Investigations in the Region West of Antas and Cuevas del Almanzora, South-Eastern Spain. Ph.D. Thesis, University Amsterdam, Amsterdam, The Netherlands, 1966; p. 124.
34. Gómez-Pugnaire, M.; Rubatto, D.; Fernández-Soler, J.; Jabaloy, A.; López-Sánchez-Vizcaíno, V.; González-Lodeiro, F.; Galindo-Zaldívar, J.; Padrón-Navarta, J. U-Pb geochronology of Nevado-Filábride gneisses: Evidence for the Variscan nature of the deepest Betic complex (SE Spain). *Lithos* **2012**, *146–147*, 93–111. [CrossRef]
35. Ruiz-Cruz, M.D.; de Galdeano, C.S.; Santamaría, Á. Geochemical Signatures and Inclusions in Apatite as Markers of a Hidden Ultrahigh-Pressure Event (Betic Cordillera, Spain). *J. Geol.* **2016**, *124*, 277–292. [CrossRef]
36. De la Roche, H.; Leterrier, J.; Grandclaude, P.; Marchal, M. A classification of volcanic and plutonic rocks using R1–R2 diagrams and major element analyses—Its relationships with current nomenclature. *Chem. Geol.* **1980**, *29*, 183–210. [CrossRef]
37. Batchelor, R.A.; Bowden, P. Petrogenetic interpretation of granitoids series using multicationic parameters. *Chem. Geol.* **1985**, *48*, 43–55. [CrossRef]
38. Pearce, J.A.; Harris, N.B.W.; Tindle, A.G. Trace element discrimination diagrams for the tectonic interpretation of granitic rocks. *J. Pet.* **1984**, *25*, 956–983. [CrossRef]
39. Nieto, J.M.; Puga, E.; Díaz de Federico, A. Late Variscan pyroclastic rocks from the Mulhacén Complex (Betic Cordillera, Spain). In *Volcaniclastic Rocks, from Magmas to Sediments*; Leyrit, H., Montenat, C.H., Eds.; Gordon and Breach Science Publishers: Amsterdam, The Netherlnds, 2000; pp. 217–234.
40. Rodríguez, J.; Pin, C.; Suárez, S.; Ortega, L.Á.; Paquette, J.L.; Ábalos, B.; Gil Ibarguchi, J.I. Hybridization of crustal magmas and direct evidence for two mantle sources during Early-Ordovician magmatism at the NW Gondwana margin. *Lithos* **2025**, *514–515*, 108171. [CrossRef]
41. Martín-Algarra, A.; García-Casco, A.; Gómez-Pugnaire, M.T.; Jabaloy-Sánchez, A.; Laborda-López, C.; Sánchez-Vizcaíno, V.L.; Mazzoli, S.; Navas-Parejo, P.; Perrone, V.; Rodríguez-Cañero, R.; et al. Paleozoic Basement and Pre-Alpine History of the Betic Cordillera. In *The Geology of Iberia: A Geodynamic Approach*; Quesada, C., Oliveira, J.T., Eds.; The Variscan Cycle: Barcelona, Spain, 2019; Volume 2, pp. 261–305.

42. Gómez-Pugnaire, M.T.; Galindo-Zaldívar, J.; Rubatto, D.; González-Lodeiro, F.; López Sánchez-Vizcaíno, V.; Jabaloy, A. A reinterpretation of the Nevado-Filábride and Alpujárride Complex (Betic Cordillera): Field, petrography and U-Pb ages from orthogneisses western Sierra Nevada, S Spain. *Schweiz. Mineral. Und Petrogr. Mitteilungen* **2004**, *84*, 303–322.

43. Linthout, K. (Vrije Universiteit Amsterdam, Amsterdam, The Netherlands). Personal communication, 2009. During a field visit with Prof. Linthout we examined an outcrop of the Ophiolitic Mélange south of Macael consisting of metapelites with chromium-rich layers and containing also decimeter-sized pockets of exceptionally pure jadeite (95–98% Jd).
44. Vissers, R.L.M. A structural study of the Central Sierra de los Filabres (Betic Zone, SE Spain), with emphasis on deformational processes and their relation to the Alpine Metamorphism. *GUA Pap. Geol.* **1981**, *15*, 1–154.
45. Puga, E.; Cruz, M.D.R.; De Federico, A.D. Polymetamorphic amphibole veins in metabasalts from the Betic Ophiolitic Association (SE Spain): Relics of ocean-floor metamorphism preserved throughout the Alpine Orogeny. *Can. Miner.* **2002**, *40*, 67–83. [CrossRef]
46. Govindaraju, K.; Potts, P.J.; Webb, P.C.; Watson, J.S. 1994 Report on Whin Sill Dolerite WS-E from England and Pitscurrie Micrograbbro PM-S from Scotland: Assessment by one hundred and four international laboratories. *Geostand. Newsl.* **1994**, *18*, 211–300. [CrossRef]
47. Williams, I.S. U–Th–Pb geochronology by ion microprobe. In: McKibben MA, Shanks III WC & Ridley WI (Eds.), Applications of Microanalytical Techniques to Understanding Mineralizing Processes. *Rev. Econ. Geol.* **1998**, *7*, 1–35.
48. Ludwig, K.R. *SQUID 1.02, a User's Manual*; Berkeley Geochronology Center Special Publication: Berkeley, CA, USA, 2001; No. 2.
49. Ludwig, K.R. *User's Manual for Isoplot/Ex Version 3.0. A Geochronological Toolkit for Microsoft Excel*; Berkeley Geochronology Center Special Publication: Berkeley, CA, USA, 2003; No. 4.
50. Ickert, R.; Hiess, J.; Williams, I.; Holden, P.; Ireland, T.; Lanc, P.; Schram, N.; Foster, J.; Clement, S. Determining high precision, in situ, oxygen isotope ratios with a SHRIMP II: Analyses of MPI-DING silicate-glass reference materials and zircon from contrasting granites. *Chem. Geol.* **2008**, *257*, 114–128. [CrossRef]
51. Black, L.P.; Kamo, S.L.; Allen, C.M.; Aleinikoff, J.N.; Davis, D.W.; Korsch, R.J.; Foudoulis, C. TEMORA 1: A new zircon standard for Phanerozoic U-Pb geochronology. *Chem. Geol.* **2003**, *200*, 155–170. [CrossRef]
52. Saccani, E.; Dilek, Y.; Marroni, M.; Pandolfi, L. Continental margin ophiolites of Neotethys: Remnants of Ancient Ocean-Continent Transition Zone (OCTZ) lithosphere and their geochemistry, mantle sources and melt evolution patterns. *Episodes* **2015**, *38*, 230–249. [CrossRef]
53. Zeng, L.; Niu, H.; Bao, Z.; Shan, Q.; Li, H.; Li, N.; Yang, W. Petrogenesis and tectonic significance of the plagiogranites in the Zhaheba ophiolite, Eastern Junggar orogen, Xinjang, China. *J. Asian Earth Sci.* **2015**, *113*, 137–150. [CrossRef]
54. Saccani, E. A new method of discriminating different types of post-Archean ophiolitic basalts and their tectonic significance using Th-Nb and Ce-Dy-Yb systematics. *Geosci. Front.* **2015**, *6*, 481–501. [CrossRef]
55. Snow, J.E.; Hart, S.R.; Dick, H.J.B. Nd and Sr isotope evidence linking mid-ocean ridge basalts and abyssal peridotites. *Nature* **1994**, *371*, 57–60. [CrossRef]
56. Sun, S.S.; McDonough, W.F. Chemical and isotopic systematic of oceanic basalts; implications for mantle composition and processes. In *Magmatism in the Oceanic Basins*; Saunders, A.D., Norry, M.J., Eds.; Special Publication Geological Society of London: London, UK, 1989; Volume 42, pp. 313–345.
57. Rampone, E.; Hofmann, A.W.; Raczek, I. Isotopic constraints within the Internal Liguride ophiolite (N. Italy): The lack of a genetic mantle–crust link. *Earth Planet. Sci. Lett.* **1998**, *163*, 175–189. [CrossRef]
58. Schaltegger, U.; Desmurs, L.; Manatschal, G.; Müntener, O.; Meier, M.; Frank, M.; Bernoulli, D. The transition from rifting to seafloor spreading within a magma-poor rifted margin: Field and isotopic constraints. *Terra Nova* **2002**, *14*, 156–162. [CrossRef]
59. Cipriani, A.; Brueckner, H.K.; Bonatti, E.; Brunelli, D. Oceanic crust generated by elusive parents: Sr and Nd isotopes in basalt-peridotite pairs from the Mid-Atlantic Ridge. *Geology* **2004**, *32*, 657–660. [CrossRef]
60. Jones, C.E.; Jenkyns, H.C.; Coe, A.L.; Stephen, H.P. Strontium isotopic variations in Jurassic and Cretaceous seawater. Geochimica et Cosmochimica. *Acta* **1994**, *58*, 3061–3074. [CrossRef]
61. Dilek, Y.; Furnes, H. Ophiolites and their origins. *Elements* **2014**, *10*, 93–100. [CrossRef]
62. Furnes, H.; Dilek, Y. Geochemical characterization and petrogenesis of intermediate to silicic rocks in ophiolites: A global synthesis. *Earth-Sci. Rev.* **2017**, *166*, 1–37. [CrossRef]
63. Furnes, H.; de Wit, M.; Dilek, Y. Four billion years of ophiolites reveal secular trends in oceanic crust formation. *Geosci. Front.* **2014**, *5*, 571–603. [CrossRef]
64. Puga, E.; Fanning, C.M.; Nieto, J.M.; De Federico, A.D. New recrystallisation textures in zircons generated by ocean-floor and eclogite facies metamorphism: A cathodoluminescence and U-Pb SHRIMP study with constraints from REE elements. *Can. Miner.* **2005**, *43*, 183–202. [CrossRef]
65. Puga, E.; de Federico, A.D.; Demant, A. The eclogitized pillows of the Betic Ophiolitic Association: Relics of the Tethys ocean floor incorporated to the Alpine Chain after subduction. *Terra Nova* **1995**, *7*, 31–43. [CrossRef]
66. Puga, E.; Nieto, J.; de Federico, A.D.; Bodinier, J.; Morten, L. Petrology and metamorphic evolution of ultramafic rocks and dolerite dykes of the Betic Ophiolitic Association (Mulhacén Complex, SE Spain): Evidence of eo-Alpine subduction following an ocean-floor metasomatic process. *Lithos* **1999**, *49*, 23–56. [CrossRef]

67. Puga, E.; de Federico, A.D.; Nieto, J.M.; Puga, M.A.D.; Martínez-Conde, J.A.R. The Betic Ophiolitic Association: A very significant geological heritage in urgent need of preservation. *Geoheritage* **2009**, *1*, 11–31. [CrossRef]
68. Alt, J.C.; Garrido, C.J.; Shanks, W.; Turchyn, A.; Padrón-Navarta, J.A.; Sánchez-Vizcaíno, V.L.; Pugnaire, M.T.G.; Marchesi, C. Recycling of water, carbon and sulfur during subduction of serpentinites: A stable isotope study of Cerro del Almirez, Spain. *Earth Planet. Sci. Lett.* **2012**, *327–328*, 50–60. [CrossRef]
69. Tera, F.; Wasserburg, G. U–Th–Pb systematics in three Apollo 14 basalts and the problem of initial Pb in lunar rocks. *Earth Planet. Sci. Lett.* **1972**, *14*, 281–304. [CrossRef]
70. Puga, E.; De Federico, A.D.; Bargossi, G.M.; Morten, L. The Nevado Filabride metaophiolitic association in the Cóbdar region (Betic Cordillera, SE Spain): Preservation of pillow structures and development of coronitic eclogites. *Geodin. Acta* **1989**, *3*, 17–36. [CrossRef]
71. Gomez-Pugnaire, M.T.; Muñoz, M. Xenolitos de metapelitas de alto grado en metabasitas: Evidencia del emplazamiento en corteza continental del magmatismo básico Nevado-Filábride (Cordilleras Béticas). *Geogaceta* **1990**, *7*, 13–15.
72. Skolotnev, S.G.; Bel'tenev, V.E.; Lepekhina, E.N.; Ipat'eva, I.S. Younger and Older Zircons from Rocks of the Oceanic Lithosphere in the Central Atlantic and Their Geotectonic Implications. *Geotectonics* **2010**, *44*, 462–492. [CrossRef]
73. Schwartz, J.J.; John, B.E.; Cheadle, M.J.; Wooden, J.L.; Mazdab, F.; Swapp, S.; Grimes, C.B. Dissolution–reprecipitation of igneous zircon in mid-ocean ridge gabbro, Atlantis Bank, Southwest Indian Ridge. *Chem. Geol.* **2010**, *274*, 68–81. [CrossRef]
74. Grimes, C.B.; John, B.E.; Cheadle, M.J.; Mazdab, F.K.; Wooden, J.L.; Swapp, S.; Schwartz, J.J. On the occurrence, trace element geochemistry, and crystallization history of zircon from in situ ocean lithosphere. *Contrib. Miner. Pet.* **2009**, *158*, 757–783. [CrossRef]
75. Pilot, J.; Werner, C.D.; Haubrich, F.; Baumann, N. Paleozoic and Proterozoic Zircons from the Mid-Atlantic Ridge. *Nature* **1998**, *393*, 676–679. [CrossRef]
76. Bortnikov, N.S.; Sharkov, E.V.; Bogatikov, O.A.; Zinger, T.F.; Lepekhina, E.N.; Antonov, A.V.; Sergeev, S.A. Finds of young and ancient zircons in gabbroids of the Markov Deep, Mid-Atlantic Ridge, 5°54′–5°02.2′ N (Results of SHRIMP-II U-Pb Dating): Implication for deep geodynamics of modern oceans. *Dokl. Earth Sci.* **2008**, *421*, 859–866. [CrossRef]
77. Valley, J.W. Oxygen isotopes in zircon. *Rev. Miner. Geochem.* **2003**, *53*, 343–385. [CrossRef]
78. Cavosie, A.J.; Kita, N.T.; Valley, J.W. Primitive oxygen-isotope ratio recorded in magmatic zircon from the Mid-Atlantic Ridge. *Am. Miner.* **2009**, *94*, 926–934. [CrossRef]
79. Grimes, C.B.; Ushikubo, T.; John, B.E.; Valley, J.W. Uniformly mantle-like d^{18}O in zircons from oceanic plagiogranites and gabbros. *Contrib. Miner. Pet.* **2011**, *161*, 13–33. [CrossRef]
80. Hoskin, P.; Black, L. Metamorphic zircon formation by solid-state recrystallization of protolith igneous zircon. *J. Metamorph. Geol.* **2000**, *18*, 423–439. [CrossRef]
81. Vavra, G.; Gebauer, D.; Schmid, R.; Compston, W. Multiple zircon growth and recrystallization during polyphase Late Carboniferous to Triassic metamorphism in granulites of the Ivrea Zone (Southern Alps): An ion microprobe (SHRIMP) study. *Contrib. Miner. Pet.* **1996**, *122*, 337–358. [CrossRef]
82. Bortolotti, V.; Principi, G. Tethyan ophiolites and Pangaea breakup. *Isl. Arc* **2005**, *14*, 442–470. [CrossRef]
83. Li, X.H.; Faure, M.; Lin, W.; Manatschal, G. New isotopic constraints on age and magma genesis of an embryonic oceanic crust: The Chenaillet Ophiolite in the Western Alps. *Lithos* **2013**, *160–161*, 283–291. [CrossRef]
84. Tribuzio, R.; Garzetti, F.; Corfu, F.; Tiepolo, M.; Renna, M.R. U–Pb zircon geochronology of the Ligurian ophiolites (Northern Apennine, Italy): Implications for continental breakup to slow seafloor spreading. *Tectonophysics* **2016**, *666*, 220–243. [CrossRef]
85. Cruz, M.D.R.; Puga, E.; De Federico, A.D. Exsolution microstructures in amphiboles from metabasalts of the Betic ophiolitic association (SE Spain). *Eur. J. Miner.* **2007**, *19*, 547–556. [CrossRef]
86. Schettino, A.; Turco, E. Breakup of Pangaea and Plate Kinematics of the central Atlantic and Atlas region. *Geophys. J. Int.* **2009**, *178*, 1078–1097. [CrossRef]
87. Jagoutz, O.; Müntener, O.; Manatschal, G.; Rubatto, D.; Péron-Pinvidic, G.; Turrin, B.D.; Villa, I.M. The rift-to-drift transition in the North Atlantic: A stuttering start of the MORB machine? *Geology* **2007**, *35*, 1087. [CrossRef]
88. Karson, J.A.; Früh-Green, G.L.; Kelley, D.S.; Williams, E.A.; Yoerger, D.R.; Jakuba, M. Detachment shear zone of the Atlantis Massif core complex, Mid-Atlantic Ridge, 30ºN. *Geochem. Geophys. Geosystems* **2006**, *7*, Q06016. [CrossRef]
89. Ildefonse, B.; Blackman, D.K.; John, B.E.; Ohara, Y.; Miller, D.J.; MacLeod, C.J. Oceanic core complexes and crustal accretion at slow-spreading ridges. *Geology* **2007**, *35*, 623–626. [CrossRef]
90. Lagabrielle, Y.; Brovarone, A.V.; Ildefonse, B. Fossil oceanic core complexes recognized in the blueshist metaophiolites of western Alps and Corsica. *Earth Sci. Rev.* **2015**, *141*, 1–26. [CrossRef]
91. Balestro, G.; Festa, A.; Dilek, Y.; Tartarotti, P. Pre-Alpine extensional tectonics of a peridotite-localized oceanic core complex in the late Jurassic, high-pressure Monviso ophiolite (Western Alps). *Episodes* **2015**, *38*, 266–282. [CrossRef]
92. Piccardo, G.B.; Guarnieri, L. Alpine peridotites from the Ligurian Tethys: An updated critical review. *Int. Geol. Rev.* **2010**, *52*, 1138–1159. [CrossRef]

93. Trommsdorff, V.; Sánchez-Vizcaíno, V.L.; Gómez-Pugnaire, M.T.; Müntener, O. High pressure breakdown of antigorite to spinifex-textured olivine and orthopyroxene, SE Spain. *Contrib. Miner. Pet.* **1998**, *132*, 139–148. [CrossRef]
94. Laborda-López, C.; López-Sánchez-Vizcaíno, V.; Marchesi, C.; Gómez-Pugnaire, M.T.; Garrido, C.J.; Jabaloy-Sánchez, A.; Padrón-Navarta, J.A.; Hidas, K. High pressure metamorphism of rodingites during serpentinite dehydration (Cerro del Almirez, southern Spain): Implications for the redox state in subduction zones. *J. Metamorph. Geol.* **2018**, *36*, 1141–1173. [CrossRef]

Disclaimer/Publisher's Note: The statements, opinions and data contained in all publications are solely those of the individual author(s) and contributor(s) and not of MDPI and/or the editor(s). MDPI and/or the editor(s) disclaim responsibility for any injury to people or property resulting from any ideas, methods, instructions or products referred to in the content.